Received: 8 November 2023 | Revised: 15 February 2024 | Accepted: 27 March 2024

DOI: 10.1111/gbi.12595

ORIGINAL ARTICLE

gebiology WILEY

Evaluating the multiple sulfur isotope signature of Eoarchean rocks from the Isua Supracrustal Belt (Southwest-Greenland) by MC-ICP-MS: Volcanic nutrient sources for early life

Jane E. Macdonald[1,2] | Patrick Sugden[1] | Matthew Dumont[1] | Kristoffer Szilas[3] | Stijn Glorie[4] | Alexander Simpson[4] | Sarah Gilbert[4] | Andrea Burke[1] | Eva E. Stüeken[1]

[1]School of Earth & Environmental Sciences, University of St Andrews, St Andrews, UK

[2]Department of Earth Sciences, University of Cambridge, Cambridge, UK

[3]Department of Geosciences and Natural Resource Management, University of Copenhagen, Copenhagen K, Denmark

[4]The University of Adelaide, Adelaide, South Australia, Australia

Correspondence
Jane E. Macdonald, Department of Earth Sciences, University of Cambridge, Downing Street, Cambridge, Cambridgeshire, CB2 3EQ, UK.
Email: jem250@cam.ac.uk

Funding information
Natural Environment Research Council; Australian Research Council

Abstract

On the anoxic Archean Earth, prior to the onset of oxidative weathering, electron acceptors were relatively scarce, perhaps limiting microbial productivity. An important metabolite may have been sulfate produced during the photolysis of volcanogenic SO_2 gas. Multiple sulfur isotope data can be used to track this sulfur source, and indeed this record indicates SO_2 photolysis dating back to at least 3.7 Ga, that is, as far back as proposed evidence of life on Earth. However, measurements of multiple sulfur isotopes in some key strata from that time can be challenging due to low sulfur concentrations. Some studies have overcome this challenge with NanoSIMS or optimized gas-source mass spectrometry techniques, but those instruments are not readily accessible. Here, we applied an *aqua regia* leaching protocol to extract small amounts of sulfur from whole rocks for analyses of multiple sulfur isotopes by multi-collector inductively coupled plasma mass spectrometry (MC-ICP-MS). Measurements of standards and replicates demonstrate good precision and accuracy. We applied this technique to meta-sedimentary rocks with putative biosignatures from the Eoarchean Isua Supracrustal Belt (ISB, >3.7 Ga) and found positive $\Delta^{33}S$ (1.40–1.80‰) in four meta-turbidites and negative $\Delta^{33}S$ (−0.80‰ and −0.66‰) in two meta-carbonates. Two meta-basalts do not display significant mass-independent fractionation (MIF, −0.01‰ and 0.16‰). In situ Re–Os dating on a molybdenite vein hosted in the meta-turbidites identifies an early ca. 3.7 Ga hydrothermal phase, and in situ Rb–Sr dating of micas in the meta-carbonates suggests metamorphism affected the rocks at ca. 2.2 and 1.7 Ga. We discuss alteration mechanisms and conclude that there is most likely a primary MIF-bearing phase in these meta-sediments. Our new method is therefore a useful addition to the geochemical toolbox, and it confirms that organisms at that time, if present, may indeed have been fed by volcanic nutrients.

KEYWORDS
Eoarchean, fluid alteration, in situ, Isua, MC-ICP-MS, sulfur isotopes

1 | INTRODUCTION

Sulfur isotopes have become a valuable tool for reconstructing environmental conditions and biological evolution throughout Earth's history. Sulfur has four stable isotopes (^{32}S, ^{33}S, ^{34}S, and ^{36}S) with abundances of 95.02%, 0.75%, 4.21%, and 0.02%, respectively, which undergo fractionation during numerous biogeochemical processes. So-called mass-dependent fractionation (MDF) occurs during kinetic and equilibrium processes and is controlled by the mass differences between isotopes (Albarède, 2011), and is described by the relationships $\delta^{33}S = 1000 \cdot ((1 + \delta^{34}S/1000)^{0.515} - 1)$ and $\delta^{36}S = 1000 \cdot ((1 + \delta^{34}S/1000)^{1.91} - 1)$, where $\delta^{3x}S = ((^{3x}S/^{32}S)_{sample}/(^{3x}S/^{32}S)_{VCDT} - 1) \cdot 1000$ and V-CDT is the Vienna-Canyon Diablo Troilite standard. Mass-independent fractionation (MIF) signatures are those that deviate from the typical MDF array. Sulfur isotope compositions are considered to represent MIF when $\Delta^{33}S$ ($= \delta^{33}S - 1000 \cdot ((1 + \delta^{34}S/1000)^{0.515} - 1)$) and $\Delta^{36}S$ ($= \delta^{36}S - 1000 \cdot ((1 + \delta^{34}S/1000)^{1.91} - 1)$) values diverge from zero (Farquhar & Wing, 2003). MDF and MIF have been particularly valuable for placing constraints on the composition of the Archean atmosphere >2.5 Ga (Johnston, 2011). Farquhar et al. (2000) first recognized that Archean sedimentary rocks preserve a MIF-S signal (expressed in both $\Delta^{33}S$ and $\Delta^{36}S$) not seen later in the rock record, signifying a permanent change in the global sulfur cycle. Since these original findings, an abundance of data has been generated verifying this Archean deviation from typical MDF (see e.g., compilation in Claire et al., 2014). The MIF-S signature seen in the Archean sedimentary record is most commonly attributed to the photolysis of SO_2 by ultraviolet radiation and has therefore become known as "smoking-gun evidence" for an anoxic atmosphere lacking an ozone shield (Farquhar et al., 2001; Pavlov & Kasting, 2002; Whitehill et al., 2015). According to this model, volcanogenic sulfur species (SO_2 and H_2S, initial $\Delta^{33}S = 0$; Siedenberg et al., 2016) are injected into the atmosphere, where they undergo photolysis generating a MIF signal that is carried by the major products, S_8 ($\Delta^{33}S > 0$) and H_2SO_4 ($\Delta^{33}S < 0$) (Claire et al., 2014; Ono et al., 2003). Additional products are organic compounds and residual SO_2 that may also be MIF-bearing (see detailed review by Halevy, 2013). Also, self-shielding of the SO_2 molecule during photolysis and polymerization reactions between the products may play a role in controlling the final distribution of isotopic compositions (Endo et al., 2022; Harman et al., 2018). These atmospheric species are rained out and are buried in sediments as sulfide and sulfate minerals, organic sulfur compounds or elemental sulfur. The greatest diversity of products and MIF signatures occurs in non-marine or shallow-marine settings where re-homogenization is minimized (Halevy, 2013). Detecting MIF-S in ancient sedimentary rocks has therefore long been taken as evidence of atmospheric-derived sulfur during the Archean. A confounding factor in this approach was the discovery of MIF during thermochemical sulfate reduction (Oduro et al., 2011), which occurs at temperatures exceeding 120°C (reviewed by Cai et al., 2022). The relevance of this process to ancient sedimentary data needs to be assessed on a case-by-case basis.

Despite its complexity, the sulfur isotope proxy remains one of the key tools for reconstructing the ancient sulfur cycle and, therefore, also carries great importance for understanding the origin and early evolution of life. Microbial sulfate reduction is an ancient energy-yielding metabolism (Ueno et al., 2008), but prior to the Paleoproterozoic Great Oxidation Event (GOE, ca. 2.3 Ga), sulfate concentrations were likely several orders of magnitude smaller than today (Crowe et al., 2014) and volcanism constituted the major source of sulfate to the biosphere (Muller et al., 2016). One may therefore speculate that a thriving early biosphere would have been enabled by volcanic sulfur sources.

The oldest proposed evidence of life on Earth goes back to ca. 3.7–3.8 Ga and is preserved in meta-turbidites and carbonate rocks in the Isua Greenstone Belt (e.g., Mojzsis et al., 1996; Nutman et al., 2016; Ohtomo et al., 2014; Rosing, 1999). Sulfur isotope analyses of banded iron formations and other schists of the Isua Greenstone Belt have indeed revealed the presence of MIF (Papineau & Mojzsis, 2006; Whitehouse et al., 2005), suggesting an atmospheric source of sulfur and supporting their interpretation as meta-sedimentary rocks. However, no sulfur isotope data so far exist from those rocks that hold the most promising biosignatures. The biogenicity of the carbonate record in particular is debated (Allwood et al., 2018; Zawaski et al., 2020), leaving the possibility that the carbonates are of abiotic hydrothermal origin. Additional multiple sulfur isotope analyses on these low sulfur content biosignature-bearing rocks would help distinguish if the major sulfur-bearing phases were derived from the atmosphere, supporting a sedimentary setting. Furthermore, if there is a signature of atmospheric sulfur input, and if life existed at that time, microbial sulfate reduction could have been a viable metabolism. To further validate this point, additional sulfur isotope analyses are required using small sample size methods.

Traditionally, sulfur isotopes are measured using gas-source isotope-ratio mass spectrometry (GS-IRMS), for which samples are converted to SO_2 or SF_6 gas (Hulston & Thode, 1965). While some initial studies using this method reported sample size requirements of 100 nmol to 5 µmol sulfur (Ono et al., 2006; Paris, Fehrenbacher, et al., 2014) more recent workers have been able to push this limit down to 20 nmol (Au Yang et al., 2016). Alternatively, an ion microprobe can be used for measuring sulfur isotopes of geological samples in situ (Mojzsis et al., 2003; Whitehouse et al., 2005), and this technique has even been optimized for finely disseminated sulfides in S-poor rock samples (Bryant et al., 2019; Marin-Carbonne et al., 2022). These in situ techniques are vital for understanding multiple generations of sulfides that can exist in Archean rocks, and for distinguishing fluid-rock interactions and diagenetic and recrystallization histories (Mojzsis et al., 2003; Whitehouse et al., 2005). Where these methodologies are not available, multi-collector inductively coupled plasma mass spectrometry (MC-ICP-MS) has been developed for triple sulfur isotope (^{32}S, ^{33}S, ^{34}S) measurements with sample size requirements down to 10 nmol of sulfur at a precision of 0.10‰ for $\Delta^{33}S$ (Burke et al., 2018; Paris et al., 2013; Rennie et al., 2018). This technique has been successfully applied to recent environmental samples

(Burke et al., 2018, Rennie et al., 2018), as well as to Neoarchean carbonate-associated sulfate (CAS) (Paris, Adkins, et al., 2014). More recently, Schurr et al. (2020) compared MC-ICP-MS to EA-IRMS for $\delta^{34}S$ measurements of calcium-sulfate minerals and CAS, finding good agreement with two orders of magnitude less sample for MC-ICP-MS. This technique therefore holds great potential for unlocking sulfur isotope records of other Archean archives, especially for researchers that may not have access to fluorination equipment or a NanoSIMS, which are still relatively rare instruments. Here we developed the MC-ICP-MS technique with an *aqua regia* leaching protocol that can be applied to shales and volcanic rocks. We applied this method to those meta-turbidite and carbonate rocks that have been put forward as key archives of early life (Nutman et al., 2016; Rosing, 1999). To further validate this method, we also analyzed a range of standards, as well as two samples of Proterozoic shale from the Torridon Group in Scotland (1.0 Ga), where more material was available and no MIF should be present. To support our interpretation of the Eoarchean sulfur isotope data, we performed detailed optical microscopy, XRF mapping, bulk elemental analyses, and geochronology of selected mineral phases, which allowed us to evaluate primary and secondary controls on the samples. Although alteration is impossible to rule out, the most parsimonious explanation of our data is a primary atmospheric source of sulfur in these rocks at 3.7 Ga, confirming the idea that organisms living at that time would indeed have had access to this nutrient source.

2 | GEOLOGICAL SETTING AND SAMPLING

2.1 | Regional geology of the Isua Supcracrustal Belt

The Isua Supracrustal Belt (ISB) is located within the Itsaq Gneiss Complex (IGC) in the southwest of Greenland (Figure 1). The complex is mainly composed of gneisses derived from tonalite-trondhjemite-granodiorite (TTG), granitic, and dioritic protoliths which have undergone multiple deformation events and high-grade metamorphism (Nutman et al., 1993). However, around 10% of the complex comprises metasedimentary, mafic, and ultramafic rocks (Nutman et al., 1996). The best-preserved examples of these varied rock types lie in the north of the complex which includes the ISB (Nutman et al., 2002). The ISB is the largest supracrustal inclusion within the IGC at 35 km long and up to 4 km wide (McGregor & Mason, 1977). Using U–Pb dating of zircon, Nutman and Friend (2009) have differentiated the ISB into two terranes: a southern ~3800 Ma terrane and a northern ~3700 Ma terrane. Both terranes contain a diverse range of rock types such as felsic schists, amphibolites of differing compositions, and banded iron formations (Nutman & Friend, 2009). Parts of the ISB have experienced only up to amphibolite facies metamorphism and contain rare areas of low strain (<5% of the belt), so these preserve features such as pillow lavas and sedimentary structures unlike other global Eoarchean terranes (Nutman et al., 2022). The presence of pillow structures and BIFs suggests deposition in a submarine setting (Appel et al., 1998). Early work revealed that the ISB underwent regional metamorphism before 3600 Ma at prograde temperatures and pressures of at least ~550°C and ~5 kbar, buried to at least 15 km depth (Boak & Dymek, 1982). Ramírez-Salazar et al. (2021) later identified three metamorphic events, including an amphibolite facies event in the Eoarchean followed by a lower amphibolite facies event in the Neoarchean and finally a later lower grade retrogression. Zuo et al. (2021) contribute further deformation evidence, possibly linked to heat-pipe tectonics during emplacement. Despite this complex metamorphic history, Isua remains an essential locality for understanding environments and potential life on the early Earth.

2.2 | ISB meta-turbidites

The meta-turbidite samples analyzed in this study (sample numbers 208288, 208290, 208293, and 208294) were collected during a field trip in 2019 from a felsic schist unit on the western side of the ISB in the ~3700 Ma terrane (Figure 1). The locality for these samples was described by Rosing (1999) as ~50 m across with predominantly 10–70 cm graded beds mixed with 10 cm slate units. The package has been interpreted as a turbidite sequence. Most notably, rocks from this locality contain graphite, which has been found to have a depleted $\delta^{13}C$ signature of −19‰. This signature could potentially represent some of the earliest evidence of microbial life on Earth (Rosing, 1999). Furthermore, one sample contains a molybdenite vein, which is intriguing because molybdenum is an essential ingredient for the evolution of life and it has been suggested to be key in the coevolution of life and environment (Anbar & Knoll, 2002; Schoepp-Cothenet et al., 2012). The specific samples targeted in this study are slates which have been previously analyzed for major and minor elements along with carbon and nitrogen isotopes and total nitrogen, sulfur, and organic carbon content (Stüeken et al., 2021).

2.3 | ISB meta-carbonates

Samples 207850(1) and 207850(2) were collected in 2022 from the eastern side of the ISB in the ~3700 Ma terrane (Figure 1). They are two separate off-cuts of a ca. 20 cm large block. Nutman et al. (2016) proposed that this outcrop locality contains primary meta-carbonate containing fossil stromatolites, which would be the earliest physical evidence of life on Earth, predating the next-oldest example of stromatolites by 200 Myr (Wacey, 2010). Nutman et al. (2016) suggest that the presence of a CO_2-rich fluid during metamorphism prevented reactions between quartz and dolomite, allowing sedimentary structures to remain intact. This mechanism, along with additional evidence such as the presence

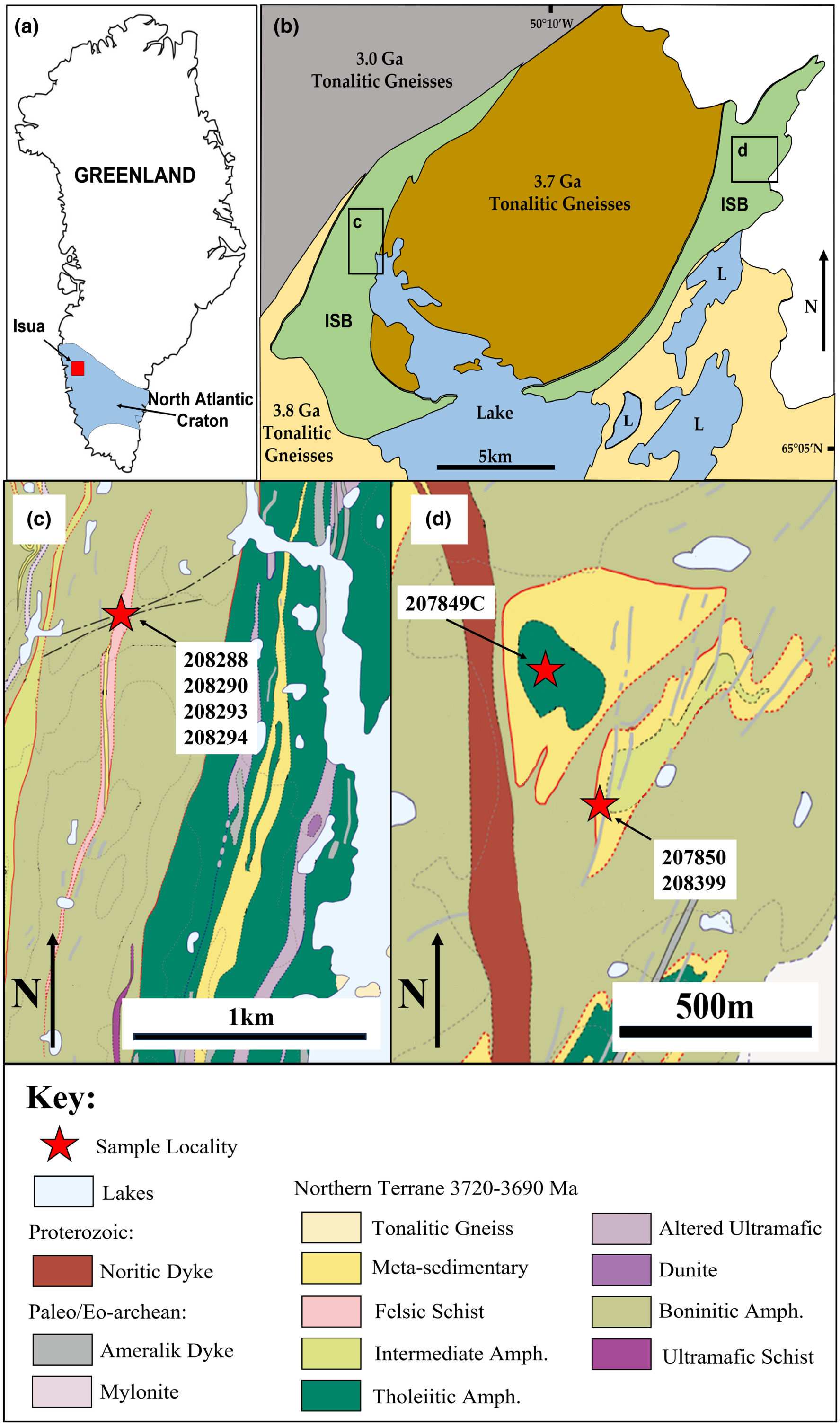

FIGURE 1 (a) Location of Isua within the North Atlantic craton in SW Greenland. Modified from Kolb et al. (2015). (b) Map of the ISB and surrounding area. (c) Geological map of sample area on the western side of the ISB. Modified from Nutman and Friend (2009). (d) Geological map of sample area on the eastern side of the ISB. Modified from Nutman and Friend (2009).

of internal laminae, trace element compositions, and adjacent shallow water storm deposits were used to argue in favour of a biogenic origin. However, these claims have been disputed by Allwood et al. (2018) using finer-scale geochemical and three-dimensional analysis. They documented characteristic trace element compositions not only in carbonate layers but also in silicate layers and therefore attributed the carbonate in this rock to metasomatic alteration rather than a primary sedimentary assemblage. This was further supported by detailed structural analysis by Zawaski et al. (2020), who concluded that the structures are boudins formed through tectonic activity rather than stromatolites. Many ISB rocks were originally interpreted as primary sedimentary carbonate but have now been linked to metasomatism (Rose et al., 1996). The use of sulfur isotopes may help to distinguish a sedimentary origin for this locality as Archean sediments should preserve a MIF-S signature.

2.4 | ISB amphibolites

We also obtained two samples of amphibolite from the ISB to serve as control samples of non-sedimentary origin. Sample 208399 is collected from the same site as the meta-carbonate described in Section 2.3, while 207849C is from an adjacent amphibolite unit. These samples have not been previously studied in the literature, so no existing data are available. As these rocks are derived from a mafic igneous protolith, no MIF-S signature is expected and should reflect the mantle signature of $\Delta^{33}S = 0$ (Siedenberg et al., 2016). As a result, these samples are used to compare meta-carbonates and meta-turbidites thought to be of sedimentary origin. Their proximity to the meta-carbonates may also be useful in identifying potential later metasomatism.

2.5 | Proterozoic control samples

To test the reproducibility of the MC-ICP-MS sulfur isotope method on whole-rock samples, the Eoarchean samples from the ISB were supplemented with two samples of late Proterozoic age (samples 180808-1 and 180808-14) from the Diabaig Formation of the Torridon Group in the northwest of Scotland. Like the ISB rocks, these samples have a complex matrix and relatively low sulfur content, making them suitable for testing the new sample preparation protocol. The samples have been previously measured for $\delta^{34}S$ (Nielson et al., 2024) using EA-IRMS. They postdate the Archean and, therefore, should show no MIF-S. As a result, they could be used to verify that the method is accurate for whole-rock samples with a complex matrix. These samples were prepared twice each to test the reproducibility of the method.

3 | METHODS

3.1 | Cutting and pulverizing

All sample preparation for sulfur isotope analyses was carried out at the School of Earth and Environmental Sciences at the University of St Andrews. The ISB meta-turbidites and the Proterozoic shales had already been powdered for a previous study (Nielson et al., 2024; Stüeken et al., 2021). Hand samples of the ISB meta-carbonates and amphibolites were cut to an appropriate size and weathered surfaces were removed using a water-cooled diamond saw. The blocks were hammered into sub-cm-sized pieces using a steel mortar and pestle. These chips were milled into a fine powder with a Fritsch Pulverisette agate ball mill. Between samples, all equipment was cleaned with deionized water and ethanol and dried with compressed air. Additionally, between samples the ball mill was run for several minutes with pre-combusted silica sand to clean out any excess residue.

3.2 | Thin section petrography

Off-cuts of all Archean samples were cut to size for thin sections and polished with grinding laps. General petrographic analysis of mineralogy and textures, including reflected light microscopy, was carried out using a Leica DM750 P polarization microscope at the University of St Andrews. Photomicrographs were taken using a Leica ICC50 W microscope camera module and processed using Leica LAS EZ imaging software.

3.3 | Bulk rock sulfur content

To determine the approximate abundance of sulfur in each sample, approximately 20 mg of sample powder, plus 5 mg of V_2O_5 powder, were weighed into 8 mm × 5 mm tin capsules (Thermo Fisher) and analyzed by flash combustion with an EA Isolink (Thermo Fisher) coupled to a MAT253 isotope-ratio mass spectrometer via a Conflo IV (Thermo Finnigan). In the EA, the combustion furnace mantling the reactor was set to 1020°C. Pure O_2 gas was injected at a flow rate of 250 mL min^{-1} for a duration of 5 s starting with the drop of the sample. The reactor was filled with 6 cm anhydrous tungstic oxide granules as an additional combustion aid, followed by 13 cm of Cu wire as a reductant of excess O_2. The gas stream was passed through a water trap filled with $Mg(ClO_4)_2$ at room temperature before entering the gas chromatography column (GC). All reagents were purchased from Elemental Microanalysis. The temperature of the GC was ramped from 60°C to 240°C to ensure complete elution of all gases. The measured SO_2 peaks were too small (<5 vs.) to obtain accurate isotopic analyses, but approximate sulfur abundances could be estimated. Abundances were calibrated against peak areas generated by pure sulfide standards IAEA-S2 and IAEA-S3. This method was also used to obtain sulfur isotope analyses by IRMS of the standard NBS-127. This standard was analyzed by MC-ICP-MS as well, providing additional cross-calibration between the two techniques.

3.4 | Sulfur leaching and purification for isotopic analyses

Wet chemistry and isotopic analyses were carried out in the St Andrews Isotope Geochemistry (STAiG) clean laboratories. Sulfur was leached from the samples with *aqua regia* as described in Xu et al. (2012). Approximately 100 mg of each whole-rock sample powder was weighed into acid-cleaned Teflon cups. To each cup, 3 mL of concentrated HCl and 1 mL of concentrated HNO_3 were added. The cups were then capped and left on a hotplate overnight at 80°C. The contents of each cup were then transferred into a 15 mL acid-cleaned Falcon tube. The samples were then centrifuged at 3900 rpm for 10 min to separate the leachate from the residue. The leachate was then transferred into clean Teflon cups. The cups were left uncapped on a hotplate overnight at 80°C to evaporate. The resulting dried solids were re-dissolved in 2 mL of 0.5 M HNO_3 and left on a hotplate at 80°C for an hour to ensure that samples were completely dissolved. The samples were then transferred into 2 mL disposable centrifuge tubes and centrifuged at 1300 rpm for 5 min to separate any remaining sediment. Using a pipette, 1.8 mL of each sample was extracted for subsequent use. Guided by approximate sulfur abundances measured by EA-IRMS (Section. 3.3), dilutions of each sample were prepared and analyzed for sulfur content using an Agilent 8900 ICP-QQQ, run with the collision cell in O_2 mode (Nakano, 2018).

An aliquot of solution containing 20–100 nmol of sulfur was pipetted into Teflon vials. These aliquots were placed on a hot plate at 104°C for a few hours until just evaporated. Residues were then re-dissolved in 4 mL 0.01% HCl and transferred into 15 mL centrifuge tubes. These solutions were then purified by anion exchange chromatography (resin AG1-X8) in a PrepFAST MC unit fitted with a 2 mL column, and a flow rate set to 2 mL min^{-1}. The resin was washed and conditioned for each subsequent sample by washing with 20 mL 1.1 M HCl, 20 mL MilliQ water, 20 mL1.6 M HNO_3, a further 20 mL 1.1 M HCl and finally conditioning with 20 mL 0.06 M HCl before sample loading. The sample matrix was washed with 30 mL MilliQ water before the sulfate fraction was collected in 12 mL of 0.5 M HNO_3. These purified solutions were dried down at 104°C, before being re-dissolved in 80 μM NaOH (250 μL of 2 μM NaOH for blanks). At the end of the sequence, the column is washed with 20 mL 1.1 M HCl and 20 mL MilliQ water before being stored in 0.1 M HCl.

3.5 | Sulfur isotope mass spectrometry

Isotope measurements were carried out with a Neptune Plus MC-ICP-MS, using sample-standard bracketing to correct for instrumental mass bias and drift. Samples were concentration-checked prior to isotope analysis and further diluted with 80 μM NaOH (the final volume of which depended on the actual number of nmol of SO_4 in the sample based on the concentration check) to achieve a matrix match with an in-house 40 μM Na_2SO_4 bracketing standard (Paris et al., 2013). Before each run, the instrument was tuned to optimize signal sensitivity and mass resolution and reduce interferences from ^{32}S–^{1}H to ^{16}O–^{16}O. This was done by adjusting and optimizing the torch position, source lenses, gas flows, and focus quad (Paris et al., 2013). Samples were run over several sessions and all samples were measured in triplicate where possible (and at least twice) to give an estimate of analytical reproducibility. Measurements are reported using delta notation calculated as follows relative to Vienna-Canyon Diablo Troilite (V-CDT), where $x = 33$ or 34:

$$\delta^{x}S = \left[\left({}^{x}S / {}^{32}S_{sample} / {}^{x}S / {}^{32}S_{V-CDT}\right) - 1\right] \times 1000$$

$\Delta^{33}S$ values were calculated using the equation:

$$\Delta^{33}S = \delta^{33}S / 1000 - \left(\left(\delta^{34}S/1000 + 1\right)^{0.515} - 1\right)$$

Samples are considered to display MIF if $\Delta^{33}S$ values fall outside the range from −0.14‰ to +0.14‰, which is based on the long-term external reproducibility of $\Delta^{33}S$ on full procedural replicates of standards using this method. Full procedural blanks (including dissolution) along with blanks from column chromatography were run alongside samples to track any potential contamination. Standard values were blank-corrected using column chromatography blanks, while sample data were corrected using full procedural blanks generated in this study (Table S1). Accuracy was evaluated with the external standards NBS-127 (barium sulfate), IAEA-SO-6 (barium sulfate), and IAEA-SO-5 (barium sulfate), as well as three in-house standards: Switzer Falls river water (Burke et al., 2018, 2019), a crushed and homogenized deep-sea coral and seawater from the North Sea—see Section 4.2.1 for the results of these tests.

3.6 | Micro-XRF element maps

To further characterize the samples, in particular, the distribution of major and minor elements that may aid in mineral identification and tracking secondary alteration, separate slabs of three meta-turbidites (208288, 208290, 208294), the meta-carbonate block, and one amphibolite sample (208399) was analyzed by micro-XRF. A Bruker M4 Tornado Plus micro-XRF instrument (Bruker Nano GmbH, Berlin) was used at the University of Copenhagen. The instrument is a non-destructive analyser that enables fast determination of elements and their distribution on a flat sample surface (Flude et al., 2017). The micro-XRF instrument uses a Rh X-ray source with a polycapillary lens that focuses the X-rays in combination with a collimator for reducing the aperture. The signal is captured with two XFlash® silicon drift detector (130 eV resolution). The beam size can go down to 20 μm and elements from Na to U can be detected (Bruker, 2023). The micro-XRF instrument detects individual elements by fluorescence X-rays (secondary X-rays) emitted when the sample is bombarded with high-energy X-rays. From Moseley's law, the peak of the lines increases approximately at the square root of the atomic number from the emitted element, so, for example, Fe has a higher intensity than Si (Wenk & Bulakh, 2016). The maximum depth of recorded fluorescence X-rays, the XRF saturation depth, varies with atomic number (Janssens et al., 2000). Minerals with heavier elements thus have a deeper XRF saturation depth than minerals with lighter elements. The XRF signals attenuate by depth and the XRF from Si has lower energy and is attenuated by the surroundings (Flude et al., 2017).

The measured samples were placed in the sample chamber under low-vacuum conditions (2 mbar) to avoid Ar absorption and to facilitate the detection of light elements. The Rh X-ray tube energy was set at 50 kV and a current of 600 μA. Measurements were performed using a 20 μm step size, 20 μm beam size, and an acquisition time of 20 ms per pixel. Spectral quantification was performed in standardless mode using M4 Tornado software. The resulting element maps show the distribution of elements and thereby textures and mineral phases can be investigated. The element maps are presented as two-dimensional image files, however, because the fluorescence X-rays come from different depths, there are some interferences in the signal that require interpretation to deduce the mineralogy at the level of each pixel.

3.7 | Bulk elemental composition

Rock chips of one amphibolite (207849C) and four off-cuts of the carbonate block were sent to Australian Laboratory Services (ALS) in Dublin, Ireland, for analysis of major, minor, and trace elements by method ME-MS61r. The meta-turbidites had previously been analyzed for major and trace elements by Stüeken et al. (2021), but rare earth elements (REEs) were added for this study by the same method ME-MS61r. This method uses hydrochloric acid, nitric acid, hydrofluoric acid and perchloric acid to digest the samples at elevated temperature. Solutions were evaporated, and residues were re-dissolved in weak nitric acid for analysis by ICP-MS. Sample reproducibility was better than 6% for most elements, except for La (17%), Mo (13%), Rb, 21%, Th (11%), Eu (10%), Pr (11%), and Sm (9%). The rock standards MRGeo08, OREAS-101-a, and OREAS 922 were used for external quality control, and here reproducibility was within 10% of expected values, except for REEs, which were within 16%.

3.8 | Powder X-ray diffraction method

A Bruker D8 Advance diffractometer was used for powder x-ray diffraction (PXRD) analyses at the University of Copenhagen. The instrument has a primary Ge111 monochromator and a LinxEye silicon-strip detector with an active surface covering 3.3°. The used radiation was from a sealed Cu tube (1.54059 Å). The measurements were made between 5° and 90° 2θ, in steps of 0.02° and a measuring time of 4 s. The reflection Bragg–Brentano technique was used with sample rotation and a fixed divergence at 0.25°. Sample preparation included crushing samples to a grain size of <45 µm and mounting the powder in a metal sample holder with a cavity of 2 mm depth. Mineral identification was done using Bruker's EVA software (DIFFRAC.EVA version 7), and the associated database with mineral diffraction data. Semi-quantitative phase analysis was achieved using curve fitting within this software.

3.9 | In situ molybdenite Re–Os dating

Element mapping revealed the presence of a molybdenite-filled vein in one of the meta-turbidite samples (Figure S1). This would be a significant host of sulfur in the rock and can be dated with Re–Os geochronology, allowing to constrain the timing of a major phase of sulfur introduction into the turbidites. In situ Re–Os isotopic analysis was conducted at Adelaide Microscopy (The University of Adelaide) using a RESOlution-LR 193 nm excimer laser ablation system (Applied Spectra), with a S155 sample chamber (Laurin Technic), coupled to an Agilent 8900x ICP-MS/MS. Analytical conditions were identical to Tamblyn et al. (2024). A gas mixture of CH_4 in He was used as the reaction gas, optimized for $^{187+14}$Os reaction rates, while suppressing interference of $^{187+14}$Re (Hogmalm et al., 2019; Tamblyn et al., 2024). N_2 gas (3.5 mL min^{-1}) was added to the carrier gas after the sample chamber to increase sensitivity (Hu et al., 2008). The following isotopes were measured, with dwell times in milliseconds between brackets: ^{34}S(2), ^{95}Mo(2), ^{185}Re(20), $^{185+14}$Re(50), ^{187}Os(50), $^{187+14}$Os(100), ^{189}Os(50), $^{189+14}$Os(100). ^{185}Re was measured as a proxy and ^{187}Re calculated assuming natural isotopic abundance. The laser fluence was set at 3.5 J cm^{-2} with a repetition rate of 5 Hz and a spot-size of 100 µm (except for the high-Re primary standard where a spot-size of 43 µm was used). Analyses included 30 s of background collection followed by 40 s of ablation. Data reduction was conducted in the LADR software (Norris & Danyushevsky, 2018) using molybdenite MDQ0252 from the Merlin deposit as the primary reference material for the Re/Os ratio calculations with an ID-TIMS ^{187}Os/^{187}Re ratio of 0.025649 ± 0.000105 (Tamblyn et al., 2024). The ^{189}Os/^{187}Os ratios were calibrated to synthetic sulfide standard NiS-3 (Gilbert et al., 2013), assuming natural isotopic abundances. Secondary reference molybdenites Q-molyhill and Jinka were used for accuracy verification with ID-TIMS ^{187}Os/^{187}Re ratios of 0.044699 ± 0.000166 (Re–Os age $= 2624 \pm 5$ Ma) and 0.02907 ± 0.00013 (Re–Os age $= 1720 \pm 8$ Ma), respectively (Tamblyn et al., 2024). A small amount of ^{187}Re reacts with CH_4 and, therefore, an interference correction was applied by calculating the $^{187+14}$Re counts from the $^{185+14}$Re counts assuming natural abundance, and subsequently subtracting the $^{187+14}$Re counts from $^{187+14}$Os (Tamblyn et al., 2024). All Re–Os dates were calculated in IsoplotR (Vermeesch, 2018) using the ^{187}Re decay constant of $1.6668 \pm 0.0034 \times 10^{-11}$ (Košler et al., 2003).

3.10 | In situ biotite Rb-Sr dating

From the meta-carbonate block, mica grains were subjected to Rb-Sr dating as an additional constraint on the metamorphic history of this unit. In situ Rb-Sr isotopic analysis was conducted at Adelaide Microscopy (The University of Adelaide) using a RESOlution-LR 193 nm excimer laser ablation system (Applied Spectra), with a S155 sample chamber (Laurin Technic), coupled to an Agilent 8900x ICP-MS/MS. Analytical conditions were identical to Glorie, Gilbert, et al. (2024). A gas mixture of N_2O was used as the reaction gas, optimized for ^{87}Sr^{16}O reaction rates (e.g., Hogmalm et al., 2017; Redaa et al., 2021). N_2 gas (3.5 mL min^{-1}) was added to the carrier gas after the sample chamber to increase sensitivity (Hu et al., 2008). The following isotopes were measured, with dwell times in milliseconds between brackets: ^{23}Na (2), ^{24}Mg (2), ^{27}Al (2), $^{29+16}$Si (2), $^{31+16}$P (2), ^{39}K (2), $^{43+16}$Ca (2), ^{55}Mn (2), $^{56+16}$Fe (2), ^{85}Rb (10), $^{86+16}$Sr (50), $^{87+16}$Sr (50), $^{88+16}$Sr (50), $^{89+16}$Y (5), $^{90+32}$Zr (5), $^{93+32}$Nb (5), all $^{x+16}$REE (5). ^{85}Rb was measured as a proxy and ^{87}Rb calculated assuming natural isotopic abundance. The laser fluence was set at 3.5 J cm^{-2} with a repetition rate of 5 Hz and a spot-size of 67 µm. Analyses included 30 s of background collection followed by 40 s of ablation. Data reduction was conducted in the LADR software (Norris & Danyushevsky, 2018) using NIST-610 as primary reference material and MDC phlogopite to correct the ^{87}Rb/^{87}Sr ratio for matrix-dependant fractionation (Glorie, Gilbert, et al., 2024). A Rb–Sr down-hole fractionation (DHF) correction was applied in LADR using the DHF behaviour of NIST-610. Secondary reference materials Bund-1b and Taratap were used for accuracy verification with reference ages of 286.2 ± 2.2 and 497.1 ± 0.6 Ma, respectively (Black, 2007; Glorie, Gilbert, et al., 2024; Glorie, Hand, et al., 2024). All Rb–Sr dates were calculated as inverse isochrons in IsoplotR (Vermeesch, 2018) using the Rb–Sr decay constant of $1.3972 \pm 0.0045 \times 10^{-11}$ a^{-1} (Villa et al., 2015). Reported inverse isochron uncertainties are fully propagated 95% confidence intervals, including the uncertainty on the decay constant, the uncertainty on the MDC reference material, and added uncertainty for overdispersion where required (calculated in IsoplotR).

4 | RESULTS

4.1 | Mineralogy and thin section petrography

For a summary of overall mineral components for all ISB samples as measured by XRD, see Table S2. Textural relationships are described in the following:

4.1.1 | ISB meta-turbidites

Samples 208288 and 208294 are both finely crystalline and composed predominantly of quartz and mica. The rocks display strong foliation defined by biotite and chlorite mica. However, chlorite is seen to replace biotite crystals indicating it formed at a later stage (Figure 2a). Sample 208288 is permeated by secondary veins of coarser quartz crystals (Figure 2b). Both samples display speckled occurrences of graphite (Figure 2c). This could be a potential source of organic-bound sulfur in the rock. Furthermore, sulfide minerals, most likely chalcopyrite, are visible under reflected light in both samples (Figure 2d).

Sample 208290, similarly to the previous sample is highly foliated and composed mainly of quartz, biotite, and chlorite. Foliated layers in this sample, however, appear more intensely deformed with several small-scale fold structures indicating a high amount of strain and deformation. This sample contains thin secondary quartz veins along with large patches of carbonate (Figure 2e). Foliation both wraps around and is disrupted by the carbonate minerals, suggested that the carbonate formed during secondary alteration or metasomatism. Graphite is again present throughout the sample as a potential sulfur source. The most common opaque minerals (Figure 2f) may be magnetite or ilmenite grains.

Meta-turbidite 208293 is the most highly altered of the four samples. The section overall has a cloudy and turbid texture indicative of alteration. It is predominantly composed of quartz and biotite with no replacement by chlorite as seen in other samples. Unlike the other meta-turbidite samples, 208293 contains zoisite and epidote group minerals which is typically associated with rocks that have undergone medium-grade regional metamorphism (Pichler & Schmitt-Riegraf, 1997). The sample also contains patches of likely secondary carbonate. No visible sulfides are seen under reflected light, and graphite is sparse.

4.1.2 | ISB meta-carbonates

Meta-carbonate samples 207850(1) and 207850(2) contain abundant carbonate, quartz, and biotite with small amounts of accessory opaques (Figure 3a,b). In line with Nutman et al. (2016), there is no evidence of tremolite. Sample 207850(2) contains minor amounts of pyrite, visible under reflected light and identifiable by its color and cubic crystal shape (Figure 3c,d). No obvious evidence for sulfate minerals such as barite and anhydrite was seen.

4.1.3 | ISB amphibolites

Amphibolite sample 208399 is mostly composed of amphibole, quartz and plagioclase feldspar with minor accessory carbonate and opaques. The sample contains large amphibole crystals >500 µm across, some of which are split into sub-grains characteristic of deformation (Figure 4a). Accessory carbonate is likely a sign of secondary alteration. Under reflected light, some of the opaque minerals can be identified as chalcopyrite (Figure 4b). Sample 207849C has a similar composition to 208399 with less amphibole and a greater abundance of quartz. An interesting feature of this sample is a large vein (ca. 0.4 mm width and at least several cm length) cross-cutting the entire section. Most of the vein is filled with zoisite (Figure 4c). Also, smaller vein structures (0.2 mm width and a few cm long) are filled in with zoisite. The large vein further contains sulfides, likely chalcopyrite and pyrite (Figure 4d). Additional sulfides are present outside of the vein. The presence of these veins and secondary sulfides along with carbonate point to later fluid infiltration into the rock.

4.2 | Sulfur isotope data

4.2.1 | Standards and blanks

Across the range of external and in-house consistency standards with δ^{34}S values ranging from −34‰ to 22‰, our method agrees well with previous literature (Böttcher et al., 2007; Brand et al., 2014; Burke et al., 2019; Kemeny et al., 2021; Paris et al., 2013; Present

FIGURE 2 Photomicrographs of meta-turbidite samples in thin section at 20×0.40 (a, c), 10×0.22 (d, f), and 4×0.10 (b, e) magnification. (a) Sample 208288 chlorite replacing biotite in ppl. (b) Sample 208288 quartz veins and patches in ppl. (c) Sample 208288 organic matter in ppl. (d) Sample 208288 sulfide mineral chalcopyrite under reflected light. (e) Sample 208290 carbonate patch disturbing foliation. (f) Sample 208290 non-sulfide opaques under reflected light. Bi, biotite; Chl, chlorite; Ch-py, chalcopyrite; Org, organic matter; Qtz, quartz.

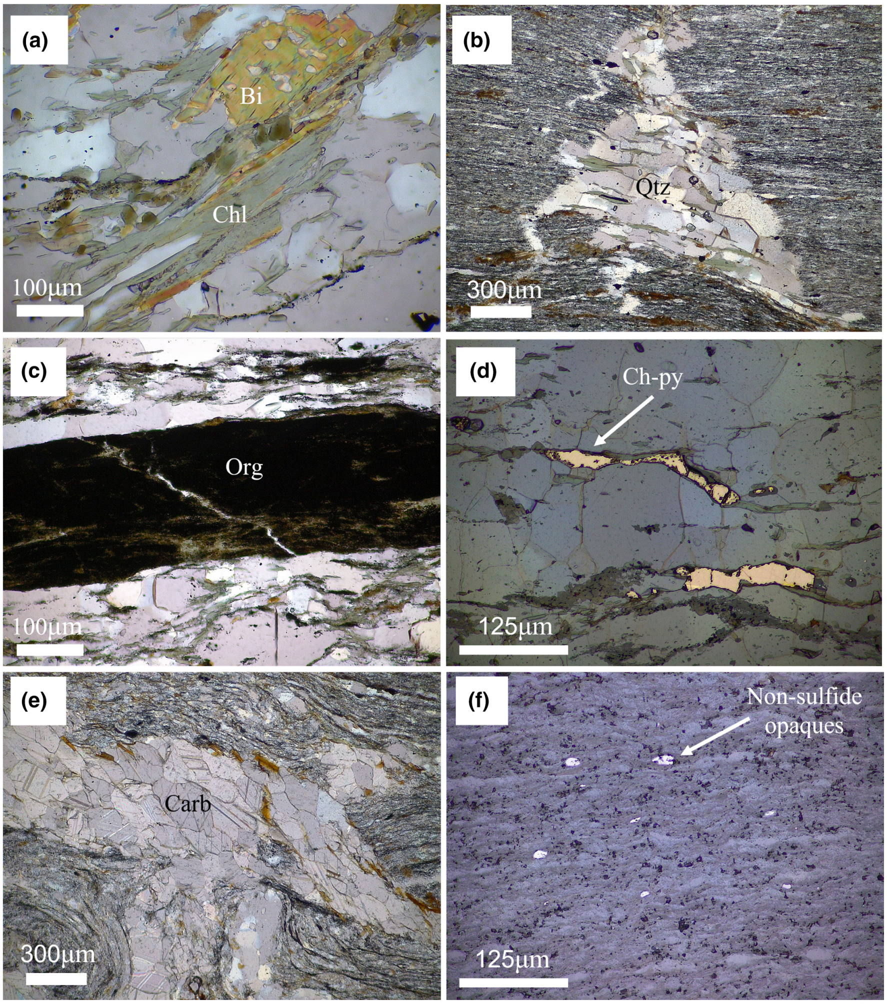

et al., 2015, Figure 5, Table 1). For each standard, the average of the full procedural replicates is within two standard deviations of the previously reported values. External reproducibility based on standards that had more than three replicates for $\delta^{34}S$ is 0.12‰ (2 SD) and for $\Delta^{33}S$ is 0.08‰, which is comparable or better than previous studies. Full procedural blanks range from 0.30 to 0.73 nmol of sulfur with an average of 0.37 ± 0.30 nmol (2 SD; $n = 8$) and had an average $\delta^{34}S = 9.20 \pm 3.49$‰ (2 SD; $n = 8$) while the blank of the prepFAST chromatographic column alone contained 0.22 ± 0.14 nmol of sulfur (2 SD; $n = 11$) and had an average $\delta^{34}S = 4.60 \pm 3.51$‰ (2 SD; $n = 11$) (Table S1).

4.2.2 | Proterozoic shales

For the two Proterozoic shales that were used for method validation (Table S3), full procedural replicates fall within the error range of each other and previously measured $\delta^{34}S$ values; however, we note that errors on existing measurements, which were obtained by EA-IRMS, are relatively large due to the low S abundance in these rocks. This indicates overall good reproducibility of the method including the digestion steps.

4.2.3 | ISB sample data

The meta-turbidites $\delta^{34}S$ values range from −1.19‰ to +0.72‰ (Table 2). All samples show a positive $\Delta^{33}S$ result ranging from 1.40‰ to 1.80‰ which is outside the 0 ± 0.14‰ threshold and, therefore, represents a MIF-S signature. The meta-carbonate samples have $\delta^{34}S$ values of 2.11 ± 0.12‰ (sample 207850(1)) and 1.53 ± 0.12‰ (sample 207850(2)). In contrast to the meta-turbidites, the meta-carbonate samples exhibit negative $\Delta^{33}S$ values of −0.80 ± 0.31‰ and −0.66 ± 0.21‰, again outside the MDF range of 0 ± 0.14‰. The amphibolite samples 208399 and 207849C display $\delta^{34}S$ values of −0.28 ± 0.12‰ and 0.41 ± 0.12‰ respectively. Sample 208399 returned a $\Delta^{33}S$ value of −0.01 ± 0.20‰ and, therefore, does not have a MIF signature. Sample 207849C has a $\Delta^{33}S$ value of 0.16 ± 0.23‰, which overlaps within error with the MDF range.

4.3 | Elemental composition and mapping

Bulk elemental compositions are shown in Table 3 and Table S4. We calculated Eu anomalies as proxies for hydrothermal input, following the procedure of Schier et al. (2020):

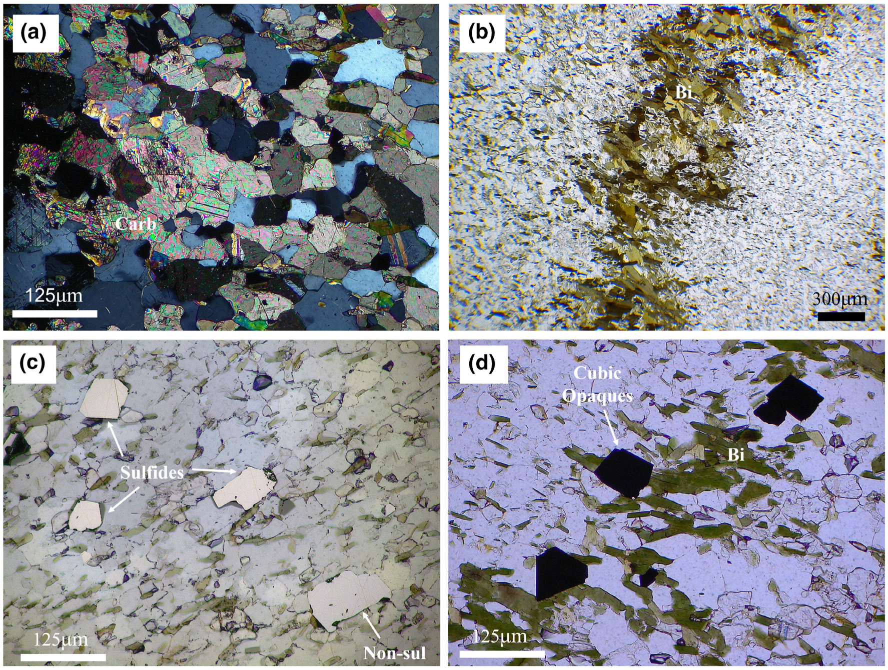

FIGURE 3 Photomicrographs of meta-carbonate sample 207850 in thin section at 10×0.22 (b–d), and 4×0.10 (a) magnification. (a) Carbonate in xpl from 207850(1). (b) Biotite layers in ppl from 207850(2). (c) Sulfides under reflected light from 207850(2). (d) Opaque mineral crystal shape in ppl from 207850(1). Bi, biotite; Carb, carbonate.

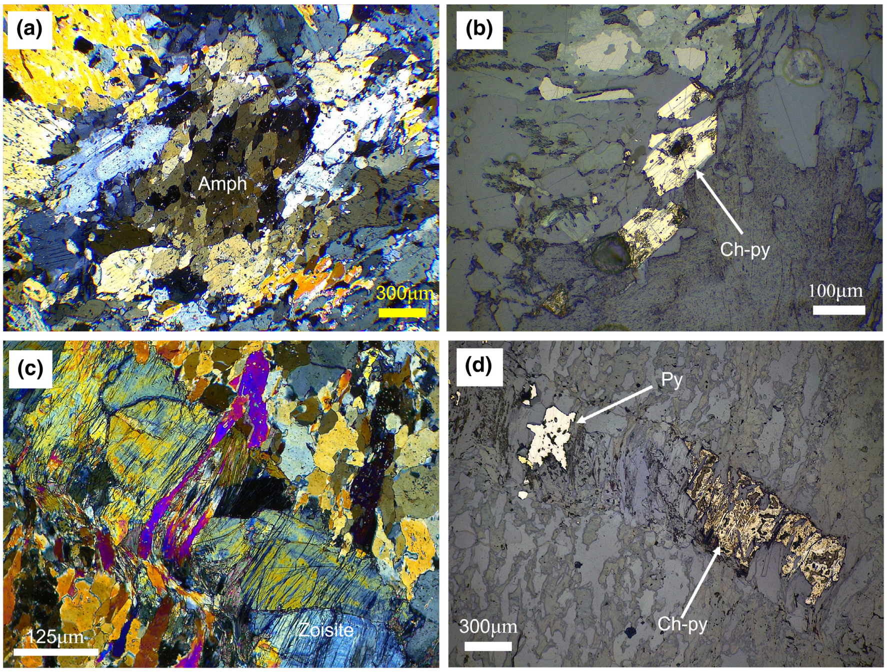

FIGURE 4 Photomicrographs of amphibolite samples in thin section at 20×0.40 (b), 10×0.22 (c), and 4×0.10 (a, d) magnification. (a) Sample 208399 large amphibole grain with sub-domains in xpl. (b) Sample 208399 chalcopyrite under reflected light. (c) Sample 2078349C large vein filled with zoisite in xpl. (d) Sample 207849C large vein filled with pyrite and chalcopyrite sulfide minerals. We note that the chalcopyrite is intergrown with pyrite and silicates and slightly sheared, giving it a "mottled" texture. Amph, amphibole; Ch-py, chalcopyrite; Py, pyrite.

$$\left(\frac{\mathrm{Eu}}{\mathrm{Eu}^{*}}\right)_{\mathrm{SN}} = \frac{\mathrm{Eu}_{\mathrm{SN}}}{\left(0.67\mathrm{Sm}_{\mathrm{SN}} + 0.33\mathrm{Tb}_{\mathrm{SN}}\right)}$$

Here SN = normalized to Post-Archean Australian Shale from McLennan (1989). The meta-turbidite samples show $(\mathrm{Eu}/\mathrm{Eu}^{*})_{\mathrm{SN}}$ of 0.869–1.970, that is, a high degree of variability (Figure 6a). In contrast, the meta-carbonate and amphibolite samples all exhibit positive Eu anomalies ranging from 1.376 to 2.980 (Figure 6b), similar to other Archean chemical sediments (Viehmann et al., 2015) and consistent with previous reports from this carbonate unit (Nutman et al., 2016). Ratios of iron to aluminum, a proxy for redox conditions, and hydrothermal input, show a mean value of 0.63 ± 0.17 for the meta-turbidites (Figure 6c), consistent with deposition under anoxic conditions (Raiswell et al., 2018; Stüeken et al., 2021). As pointed out by Raiswell et al. (2018), hydrothermal Fe enrichments are typically manifested in Fe/Al ratios exceeding 2.0, which is not the case in our samples. We therefore tentatively propose that these values were not strongly affected by hydrothermal alteration. For the meta-carbonate, four measurements cluster around a mean of 3.94 ± 1.48 with one outlier at 191.43. The amphibolite shows a value of 3.75, which is higher than the Fe/Al ratio of modern oceanic crust (1.03;

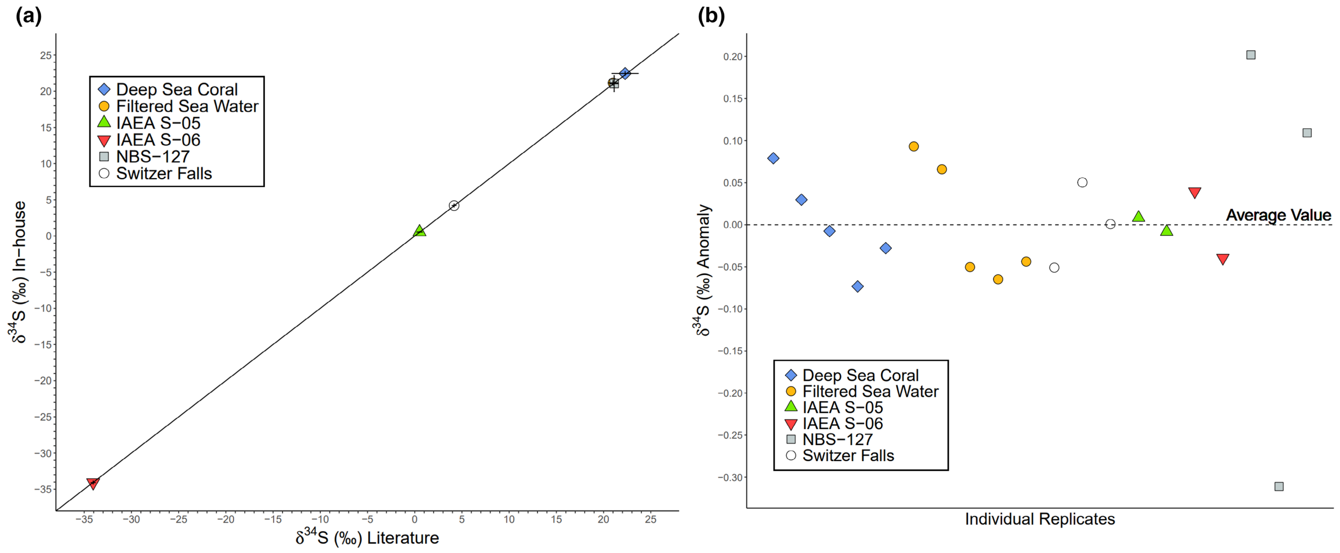

FIGURE 5 (a) Average δ^{34}S values obtained for standards in this study vs. literature values (Böttcher et al., 2007; Burke et al., 2019; Paris et al., 2013). (b) δ^{34}S anomalies of individual replicates measured relative to average standard values obtained in this study.

TABLE 1 Sulfur isotope data for external and in-house standards.

Standard	δ^{34}S (‰)	$\pm 2\sigma$[a]	δ^{33}S (‰)	$\pm 2\sigma$[a]	Δ^{33}S (‰)	$\pm 2\sigma$[a]
NBS127						
This study (MC-ICPMS)	20.75	0.12	10.70	0.26	0.07	0.23
This study (EA-IRMS)	21.43	0.54	–	–	–	–
Brand et al. (2014)	21.12	0.22	–	–	–	–
IAEA-SO-6						
This study	−34.11	0.12	−17.58	0.18	0.13	0.20
Brand et al. (2014)	−34.05	0.08	–	–	–	–
Switzer Falls						
This study (1)	4.15	0.17	2.20	0.19	0.06	0.20
This study (2)	4.25	0.12	2.24	0.19	0.05	0.20
Burke et al. (2019)	4.17	0.11	–	–	0.01	0.10
Kemeny et al. (2021)	4.2	0.4	–	–	–	–
Seawater						
This study	21.08	0.12	10.93	0.18	0.12	0.20
Böttcher et al. (2007)	21.00	0.13	–	–	–	–
Deep sea coral						
This study	22.38	0.12	11.53	0.18	0.06	0.20
Present et al. (2015)	22.38	1.12	–	–	–	–

[a] Errors represent the larger of the external reproducibility (2 SD of standards).

White & Klein, 2014) and may thus indicate hydrothermal Fe addition. As provenance indicators, we used Ni/Co and Th/Sc ratios (Ptáček et al., 2020), and found the amphibolite as well as the meta-carbonate to cluster close to the composition of modern oceanic crust (Figure 6d). This contrasts with the composition of the meta-turbidites, which appear to include relatively greater proportions of both ultramafic and felsic crust. We stress that secondary processes can alter these ratios. This interpretation is therefore tentative. Another noteworthy geochemical feature is Ba concentration above the limit of the detector (>1 wt.%) in two meta-carbonate analyses, likely indicating the presence of Ba-carbonate or possibly Ba-rich mica; as noted above, no barite was detected by XRD or microscopy.

Element maps of the meta-turbidites (Figure S1a,b in Appendix S3) are consistent with graded lamination and variable mixing between clays and sand particles. Sample 208290 shows lamina-parallel enrichments in Ca (Figure S1a), probably due to the presence of (possibly secondary) carbonate. Sample 208294 contains a lamina-parallel enrichment in Mo (Figure S1b), likely reflecting a secondary injection

TABLE 2 Sulfur isotope data for ISB samples.

Sample	TS (ppm)	δ^{34}S (‰)	±2σ[a]	δ^{33}S (‰)	±2σ[a]	Δ^{33}S (‰)	±2σ[a]
Meta-turbidites							
208288	2260	0.72	0.14	2.18	0.18	1.80	0.20
208290	57	−0.25	0.12	1.27	0.18	1.40	0.20
208293	17	−1.19	0.12	0.79	0.18	1.40	0.20
208294	2296	0.31	0.22	1.70	0.18	1.55	0.25
Meta-carbonates							
207850(1)	26	2.11	0.12	0.28	0.27	−0.80	0.31
207850(2)	41	1.53	0.12	0.12	0.19	−0.66	0.21
Amphibolites							
208399	276	−0.28	0.12	−0.15	0.18	−0.01	0.20
207849C	36	0.41	0.12	0.37	0.24	0.16	0.23

[a] Errors represent the larger of the external reproducibility (2 SD of standards).

of molybdenite. Some of the molybdenite from this rock was used for in situ Re–Os dating. Among the amphibolites, sample 208399 shows a clotted texture (Figure S2a), likely reflecting metamorphic recrystallization of original magmatic minerals. Stringers of Si enrichment are probably the result of minor secondary quartz veins. Sample 207849, which displays greater proportions of quartz/zoisite veining at hand sample scale, also shows strongly Si-enriched bands in elemental maps (Figure S2b). Lastly, the elemental map of the meta-carbonate sample reveals banding of quartz (Si) and carbonate (Ca, Fe, Mg) (Figure S2c). Strongly Al-enriched laminae may reflect stylolites.

4.4 | In situ Re–Os geochronology results

All data obtained from the Re–Os analyses are provided in Appendix S1. For the reference materials, common Os was below detection limits and, therefore, Re–Os dates were directly calculated as weighted mean ages from the ^{187}Re/$^{187+14}$Os ratios. The obtained in situ Re–Os dates of 2628 ± 8 and 1712 ± 11 Ma for the Q-molyhill and Jinka reference molybdenites, respectively (Figure 7a,b), are in excellent agreement with their ID-TIMS reference ages. Hence, the applied calibration method produces accurate Re–Os dates.

The molybdenite vein targeted for in situ Re–Os geochronology stands out in the XRF map shown in Figure S1 in Appendix S3. It has Re concentrations between ~0.5 and 3 ppm. Common Os was negligible, resulting in ^{189}Os/^{187}Os ratios <0.05 for 16 out of 17 analyses. Consequently, Re–Os dates were calculated directly from the ^{187}Re/$^{187+14}$Os ratios for these 16 analyses. Thirteen analyses gave consistent Re–Os dates, resulting in a weighted mean Re–Os date of 3695 ± 234 Ma (MSWD = 0.02; Figure 7c). The three outlier analyses, which were obtained near the edge of the molybdenite vein, define a secondary population with a weighted mean Re–Os date of 2668 ± 295 Ma (MSWD = 0.05, Figure 7c). Alternatively, an isochron regression through all data, excluding the three younger outliers, anchored to a present-day initial ^{188}Os/^{187}Os ratio set at 6.74 ± 1.00, produced a Re–Os date of 3662 ± 214 Ma (Figure 7d).

4.5 | In situ Rb–Sr geochronology results

Detailed results from the Rb-Sr analyses are presented in Appendix S2. MDC phlogopite was used to correct the Rb/Sr ratio for matrix-dependant fractionation, using the method described in Glorie, Gilbert, et al. (2024). The reference age for MDC is 519.4 ± 6.5 Ma and the inverse isochron was anchored to an initial ^{86}Sr/^{87}Sr ratio of 1.3773 ± 0.0013, constrained from a diopside (low-Rb mineral) that occurs in the same location (Hogmalm et al., 2017) (Figure 8a). The offset in the measured isochron lower intercept Rb/Sr ratio compared to the reference value, calculated from the Rb/Sr age for MDC, was used to correct the Rb/Sr ratios for all other analyzed samples. For the Bund-1b and Taratap secondary reference materials (Figure 8b,c), biotite, K-feldspar, and plagioclase (± apatite) were analyzed for Rb/Sr and Sr/Sr ratios, yielding matrix-dependant fractionation corrected inverse isochron dates of 286.8 ± 2.1 and 499.5 ± 3.6 Ma, respectively. These dates are in excellent agreement with the reference dates of 286.2 ± 2.2 and 497.1 ± 0.6 Ma, respectively (Black, 2007; Glorie, Gilbert, et al., 2024), supporting accurate age calculations.

For the Isua meta-carbonate, the Rb–Sr data define two isochron arrays with 30 analyses constraining a Rb–Sr date of 1702 ± 30 Ma (MSWD = 1.3) and 16 analyses constraining a Rb–Sr date of 2214 ± 62 Ma (MSWD = 1.3) (Figure 8d).

5 | DISCUSSION

5.1 | Evaluating the effectiveness of the MC-ICP-MS method

All standards produced accurate values in agreement with previous measurements in the literature, with reproducibility comparable or better than previous studies (Table 1), illustrating the accuracy and

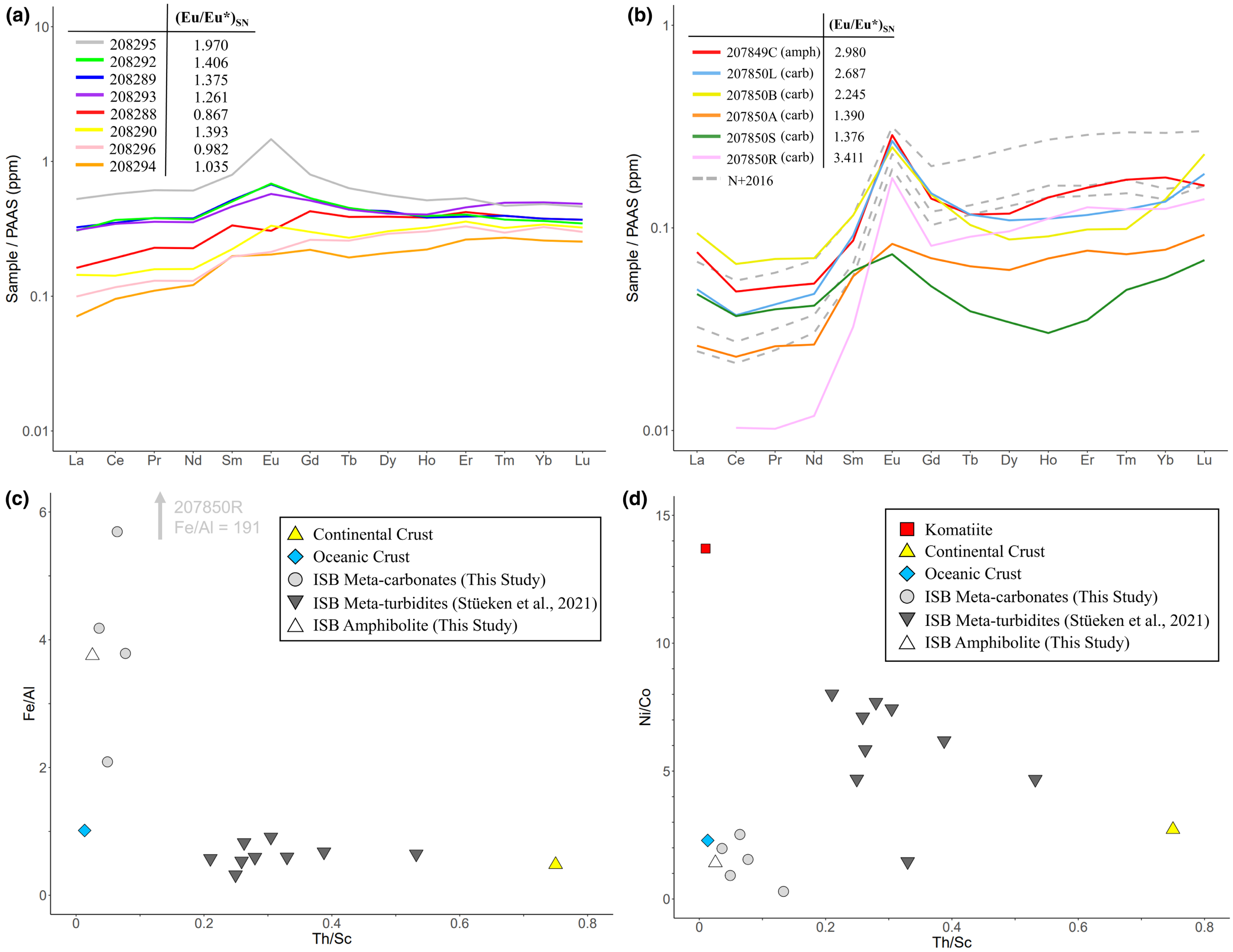

FIGURE 6 Trace element data. (a) REE patterns and Eu anomalies for ISB meta-turbidites. (b) REE patterns and Eu anomalies for ISB meta-carbonates and amphibolite. Dashed grey lines are stromatolite data replotted from Nutman et al. (2016), labelled N+2016. All REE data are normalized to Post-Archean Australian Shale from McLennan (1989). $(Eu/Eu^*)_{SN}$ calculated after Schier et al. (2020). (c) Fe/AL vs. Th/Sc. (d) Ni/Co vs. Th/Sc. Values for komatiite, continental crust and oceanic crust taken from Ptáček et al. (2020), Rudnick and Gao (2014) and White and Klein (2014), respectively.

precision of this method. Similarly, the Proterozoic shale samples fell within the error range for previously measured values (Nielson et al., 2024; Table S3), and they did not display MIF, as expected for the Mesoproterozoic. Of note is a slight bias to positive $\Delta^{33}S$ in the standards and replicate Proterozoic samples, with the average value across all standards for $\Delta^{33}S = 0.06 \pm 0.08‰$ (2 SD; $n = 20$) and the average value across the Proterozoic shale samples for $\Delta^{33}S = 0.07 \pm 0.10‰$ (2 SD; $n = 4$). Although we do not yet know the reason for this slight positive bias, we note that $\Delta^{33}S$ is still within the error of zero and is much smaller than the signals measured in this study, so it does not impact on our conclusions. In consistency with these results, we interpret anything within 0.14‰ of 0‰ as representing mass dependent fractionation. Future work will investigate potential causes for this slight positive $\Delta^{33}S$.

For replicate analyses of the same ISB solution on the MC-ICP-MS, we obtained average errors of 0.14‰ for $\delta^{34}S$ (2σ) and 0.23‰ for $\Delta^{33}S$ (2σ), which is slightly improved over ion microprobe studies (Muller et al., 2016; Papineau & Mojzsis, 2006). Collectively, these results give confidence in the accuracy and precision of our analytical method. Procedural blanks prepared alongside the ISB produced an average of 0.37 ± 0.30 nmol (2 SD; $n = 8$) of sulfur with the largest blank being 0.73 nmol. The prepFAST column chemistry blanks have an average sulfur content of 0.22 ± 0.14 nmol (2 SD; $n = 11$) (Table S1). Overall, our complete procedural blanks were thus only slightly larger than prepFAST column chemistry alone, but comparable with existing studies using column chemistry and sulfur isotope measurement by MC-ICP-MS with values ranging from 0.16–0.60 nmol and an average of 0.38 ± 0.38 (2 SD; $n = 5$, Paris, Adkins, et al., 2014). Given our typical sample size was 50 nmol, this blank represents only ~0.74% of the sample, therefore, the blanks are not a concern for the whole-rock digestion method, making it applicable to samples with very low sulfur contents (a few tens of μg/g in our case). Since *aqua regia* is an oxidizing agent, it is likely to dissolve organic-bound sulfur and sulfide minerals, and those were probably the main sulfur phases in our samples. *Aqua regia* does not fully dissolve barite (Abbasi et al., 2016); however, barite was not visible in

TABLE 3 Major and minor element data for meta-carbonates and one amphibolite sample.

	Al	Ba	Ca	Co	Cr	Cs	Cu	Fe	Ga	Hf	K	Mg	Mn	Mo
Meta-turbidite														
208288	6.9	100	0.82	14.3	51	0.76	59.6	4.68	15.55	2.3	0.85	1.07	565	0.36
208289	8.22	120	1.1	16.9	19	1.31	0.2	4.92	22.7	3.3	0.62	1.7	777	<0.05
208290	6.33	200	2.37	3.5	45	1.35	4.1	2.03	15.6	2.1	3.21	0.52	1290	0.07
208291	8.86	250	2.93	9.4	89	1.62	<0.2	4.75	23.2	2.6	3.58	1.42	1290	<0.05
208292	9.23	250	1.47	9.3	97	1.32	<0.2	5.49	24	3.4	3.83	1.69	1400	<0.05
208293	7.83	120	2.78	12.6	123	1.65	<0.2	4.51	21.5	3.3	2.34	1.86	1720	0.07
208294	5.92	40	0.83	21.7	41	0.78	80.9	3.83	10.1	3.1	0.59	0.76	428	0.46
208295	9.04	350	2.85	11.3	84	6.59	<0.2	7.45	23.2	0.8	4	1.04	929	0.09
208296	9.19	310	0.4	15.6	97	0.5	8.5	8.37	23.1	3.4	2.31	1.68	2510	0.14
Amphibolite														
207849C	2.18	20	7.54	32.5	129	0.2	12	8.18	4.05	0.3	0.04	4.71	3660	0.26
Meta-carbonate														
207850A	1.22	910	8.6	11.4	88	0.49	1.1	5.1	2.5	0.3	1.07	2.69	4060	0.07
207850B	1.26	>10,000	4.71	17	65	0.72	0.3	4.77	2.76	0.4	0.68	1.84	3220	0.09
207850L	0.94	>10,000	7.38	9.4	43	0.64	0.6	5.35	2.08	0.3	0.48	1.94	4240	0.08
207850S	1.47	4950	0.64	26.9	93	0.84	12.8	3.07	2.94	0.4	1.23	0.51	943	0.15
207850R	0.07	170	0.19	44.2	7	0.18	1.6	13.4	1.08	<0.1	0.02	0.04	312	0.45

Note: Data for the meta-turbidites are taken from Stüeken et al. (2021). The major elements Al, Ca, Fe, K, Mg, Na, and Ti are in weight %; all other elements are in ppm.

our samples and not detected by XRD (Table S2, Section 4.1.2), and so this issue would likely not be relevant for this study. Additional method development would be required for rock samples containing significant barite. The data presented here are most likely dominated by sulfide minerals and possibly organic-bound sulfur.

5.2 | Comparisons to existing Archean sulfur isotope data

Our ISB meta-turbidite data (both Δ^{33}S and δ^{34}S) align well with previously published data from banded iron formations (BIFs) and garnet-biotite schists in the ISB reported by Papineau and Mojzsis (2006) (Figure 9a). Their measurements were made using an ion microprobe targeting the individual sulfide minerals cubanite, chalcopyrite, pyrite, and pyrrhotite. Those sulfides were largely taken from meta-sedimentary units in the north-eastern segment of the ISB with one sample locality matching the western felsic schist unit examined in this study.

This similarity suggests that the sulfur in the meta-turbidites, BIFs, and garnet-biotite schists in the ISB may have come from the same source. The presence of MIF indicates an atmospheric contribution that was generated in an oxygen-poor atmosphere and it would imply that volcanism delivered S-metabolites to life, if present. More specifically, the positive Δ^{33}S values suggest that the atmospheric carrier of the MIF signal was elemental sulfur (S_8) that eventually became incorporated into sediments as sulfide (Ono et al., 2003). A sedimentary origin for these Eoarchean rocks is therefore plausible. In terms of δ^{34}S, the meta-turbidites show a very limited spread, consistent with Eoarchean δ^{34}S literature values ranging from ~−7.5‰ to 8‰ (Morrison & Mojzsis, 2020 and references therein). This narrow spread contrasts with the Neoarchean (range from ~−25‰ to 37‰) and may reflect a relatively small sulfur reservoir in seawater with limited scope for biological isotope fractionation (Morrison & Mojzsis, 2020). This interpretation is consistent with the inferred anoxic conditions based on Fe/Al ratios (Figure 6c). However, the sulfur isotope data from these rocks alone cannot rule out post-depositional introduction of younger Archean sulfur with a MIF signal. We will further address this issue below (Section 5.3).

The meta-carbonate rocks exhibit a negative Δ^{33}S signature, unlike the ISB meta-turbidites, schists and BIFs (Figure 9a,b). Similar negative Δ^{33}S values have been documented from Archean barite deposits at 3.25–3.55 Ga (Bao et al., 2007; Farquhar et al., 2000; Roerdink et al., 2012; Ueno et al., 2008) (Figure 9a). As stated in Section 4.1.2, no barite was identified in the thin section or by XRD. Furthermore, since our aqua regia leaching protocol is not optimized for barite, and since sulfide minerals were visible in the samples, the negative Δ^{33}S values are most likely sulfide-hosted. In this case, they may reflect a distinct source of sulfur (temporal or spatial) compared to the meta-turbidites, schists, and BIFs. The most plausible explanation for these values is reduction of seawater sulfate. Transfer of negative Δ^{33}S from sulfate to sulfide has been well documented in slightly younger Paleoarchean successions at 3.5–3.2 Ga, where it is usually attributed to microbial sulfate reduction (e.g, Roerdink et al., 2013; Ueno et al., 2008). In fact, this mechanism may explain many occurrences of negative Δ^{33}S values in pyrite throughout the Archean (e.g., Kamber &

Na	Nb	Ni	P	Pb	Rb	Sc	Sr	Ta	Th	Ti	U	V	Y	Zn	Zr
2.58	2.6	88.5	310	1.7	38.8	6.5	105.5	0.21	2.52	0.221	0.6	35	7.3	36	87
4.29	4.1	24.7	440	2.1	30.5	9.7	202	0.31	3.2	0.365	0.7	70	10.5	95	119
0.12	2.9	16.4	330	1.4	102.5	8.1	39.4	0.23	2.02	0.234	0.6	47	7.7	18	76
0.46	4.3	66.9	470	2.4	121	11.9	98.7	0.3	3.08	0.36	0.7	72	9.8	46	94
0.35	4.5	71.5	490	1.7	133	12.3	35.8	0.33	3.44	0.387	0.7	78	9.8	54	119
1.44	4	101	440	2.7	82.3	12	134.5	0.31	2.52	0.349	0.7	75	9.5	54	115
2.76	2.7	101.5	350	1.6	33.9	5	83.9	0.25	2.66	0.196	0.9	22	5.7	28	110
0.39	3.5	66	400	3.3	225	9.4	296	0.26	2.47	0.319	0.7	65	10	66	32
1.2	4	116	440	1.1	57	10.8	31.4	0.3	3.29	0.338	0.7	66	20.6	59	115
0.18	0.4	45.9	70	5	3.4	10.2	36.8	0.15	0.26	0.046	0.1	42	5.5	155	6.5
0.03	0.5	22.5	40	1.1	25.8	5	21.6	0.22	0.18	0.042	0.1	22	2.5	20	8.3
0.01	0.5	26.3	40	1	22.8	3.5	63.6	0.09	0.27	0.06	0.1	20	3.9	17	12.8
0.01	0.4	23.7	40	1.2	19.2	2.8	95.9	0.1	0.18	0.042	0.1	15	4.9	16	9.2
0.04	0.5	24.7	40	1	38.4	5.3	7.9	0.08	0.26	0.056	0.1	24	1	19	13
0.01	0.2	13	20	3	2.7	0.3	3	0.1	0.04	<0.005	0.4	6	4.8	5	0.8

Whitehouse, 2007; Kaufman et al., 2007; Mishima et al., 2017; Ono et al., 2003; reviewed by Claire et al., 2014; Johnston, 2011). We cannot infer the presence of this metabolism from our data alone (Δ^{36}S measurements or a larger sulfate reservoir enabling larger MDF would be needed), but it is a plausible explanation and would confirm the volcanic supply of a key metabolite for the early biosphere at that time. The presence of MIF in the meta-carbonates may reflect a sedimentary origin for these rocks, consistent with the REE data (see Allwood et al., 2018; Nutman et al., 2016, for further debate on this topic), but as with the meta-turbidites, we cannot easily rule out post-depositional introduction of younger Archean sulfur with a MIF signature (Section 5.3).

5.3 | Evidence and effects of metamorphism and alteration

Processes undergone by the ISB rocks such as subsequent metamorphism and alteration have the potential to modify original sulfur isotope signatures and, therefore, must be carefully considered. Increasing metamorphic grade has been shown to impart a positive fractionation on δ^{34}S of up to 2–3‰ at high-grade conditions (amphibolite or above; Bucholz et al., 2020). Furthermore, regional metamorphism may be capable of homogenizing sulfur pools and thus reduce the Δ^{33}S MIF signature seen in Archean meta-sedimentary sulfide minerals (Cui et al., 2018). The abundance of amphibole and the absence of high-grade mineral associations such as sillimanite and K-feldspar confirm that the samples experienced up to amphibolite facies conditions, and hence some fractionation in δ^{34}S due to metamorphism may have occurred, but since the metamorphic fractionation 2–3‰ is overall smaller than microbial sulfate reduction (up to 70‰; Sim et al., 2011), it does not impact our interpretation.

Of greater concern is secondary alteration of the MIF-S sulfur isotope signature by fluids. Confirmation of alteration of the ISB rocks is indicated by the presence of replacement chlorite, secondary carbonate and vein structures filled by quartz, sulfides, and zoisite (Figure 4, Figure S1). The replacement of biotite by chlorite is a common reaction in many rocks and is observed in the meta-turbidites in this study (Section 4.1.1). In igneous rocks, chlorite is usually associated with hydrothermal alteration; however, it can also form during regional metamorphism (Shabani, 2009). The ISB meta-turbidites are amphibolite facies rocks and therefore are not expected to contain metamorphic chlorite that typically reflects greenschist metamorphic grade; therefore, the presence of chlorite indicates that it is a secondary feature that was most likely introduced by fluids (Chipman, 1989). The addition of hydrothermal fluid has been linked to retrogression and formation of chlorite in metamorphic complexes, so chlorite is potentially an indicator of hydrothermal alteration for the ISB (Cao et al., 2017). Furthermore, both the meta-turbidites and amphibolites contain unexpected carbonate. The patchy and vein-like structures indicate a secondary nature for this carbonate. Carbonate alteration caused by metasomatism is pervasive throughout the ISB and not linked to a singular event, highlighting multiple opportunities for fluid alteration to effect isotope values (Polat & Hofmann, 2003). The zoisite seen in amphibolite 207849C occurs in veins suggesting

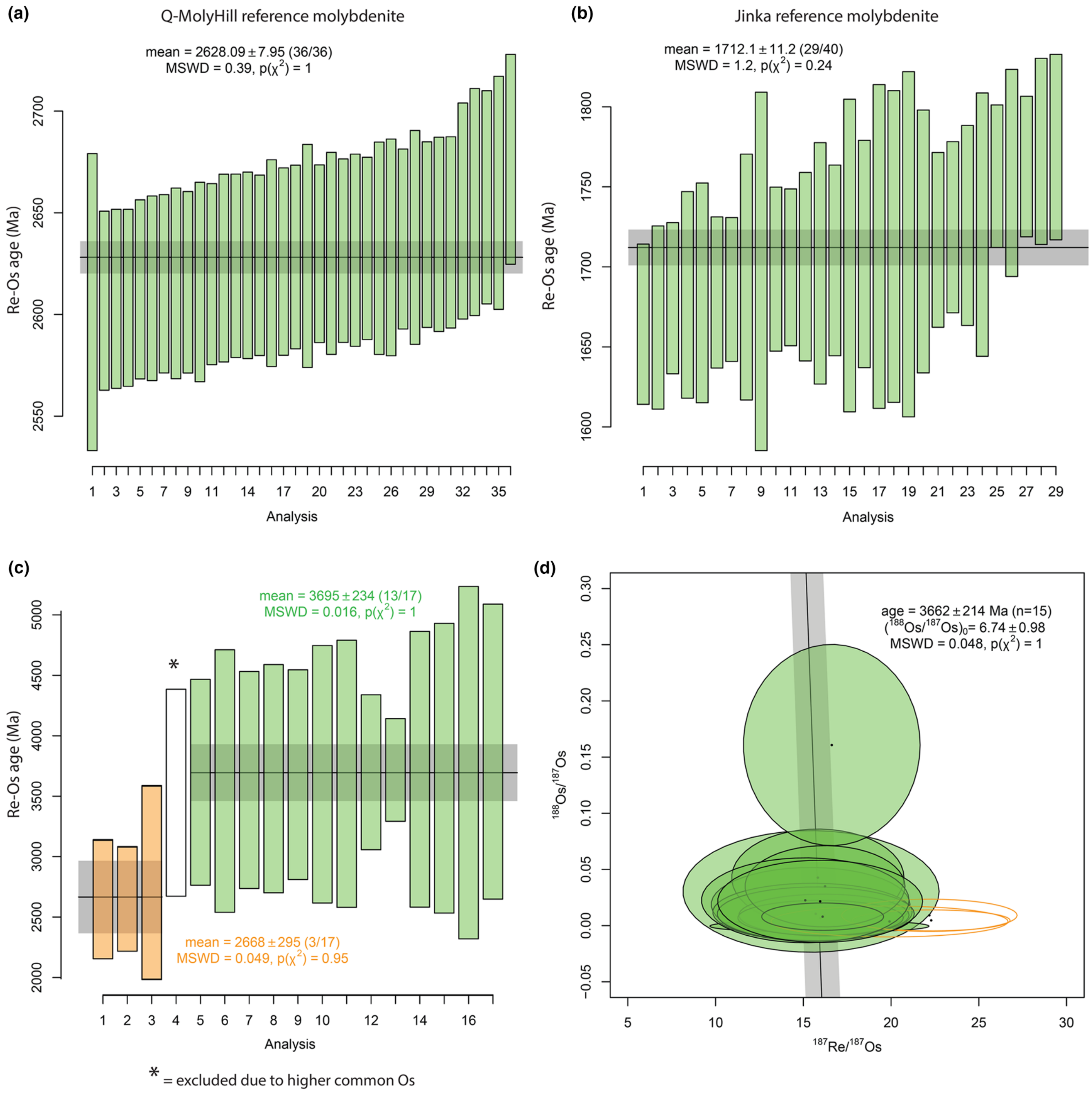

FIGURE 7 Re–Os geochronology data for reference materials and the Isua molybdenite vein. (a, b) Illustrate analytical reproducibility for two reference materials. (c) Shows the measured ages for the interior (3695 ± 234 Ma, MSWD = 0.02) and edge of the molybdenite vein (2668 ± 295 Ma, MSWD = 0.05). (d) Shows and alternative isochron regression through all data, excluding the three younger outliers, anchored to a present-day initial $^{188}Os/^{187}Os$ ratio set at 6.74 ± 1.00, which produced a Re–Os date of 3662 ± 214 Ma.

that it is also secondary. The appearance of sulfides filling vein structures and their recrystallized morphologies could be a sign that sulfur has been added to this sample from an outside source (although it is possible that the vein formed from remobilization of primary sulfur that was already indigenous to the rock). Lastly, the presence of chalcopyrite ($CuFeS_2$) is typically associated with hydrothermal fluids rich in copper (Haldar, 2017). Both the meta-turbidites and amphibolites appear to contain molybdenum or copper sulfides suggesting that these rocks experienced hydrothermal input either during or after deposition. Shales at this locality display a correlation between Cu and total sulfur abundance (Stüeken et al., 2021), and the presence of chalcopyrite and molybdenite at the meta-turbidite locality is supported by previous mapping surveys of the outcrop (Rosing, 1999).

These observations collectively raise several potential issues with the measured sulfur isotope signatures. The Re–Os dates obtained from the molybdenite vein provide a constraint on at least some of the hydrothermal history of these rocks. We obtained two ages: 3695 ± 234 Ma for the interior of the vein and 2668 ± 295 Ma for the edge (Figure 7c). The former age overlaps with the estimated

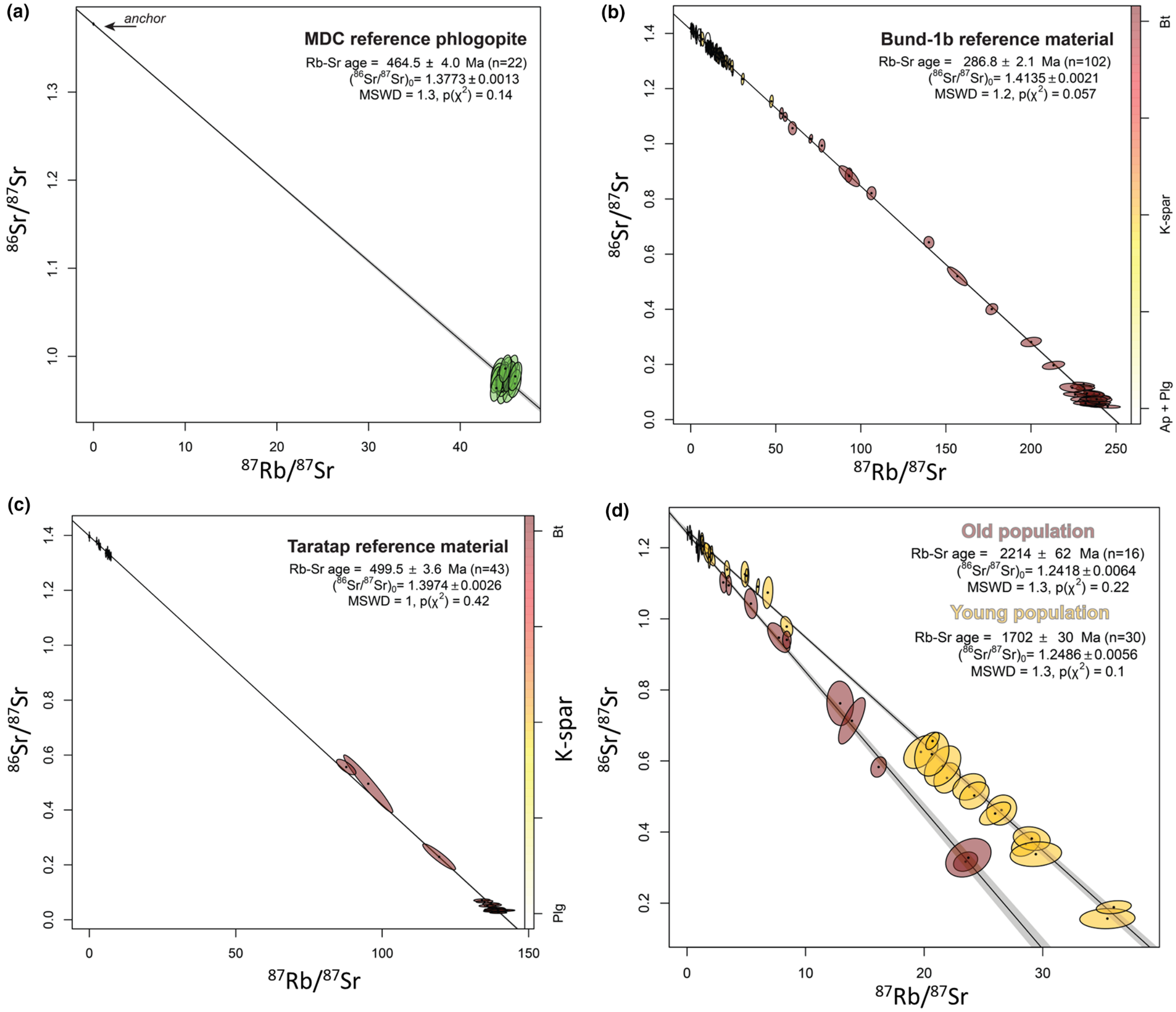

FIGURE 8 Rb–Sr geochronology data for reference materials and meta-carbonate samples. (a) MDC phlogopite used for calibration; (b) Bund-1b quality control reference material; (c) Taratap quality control material; (d) results for Isua meta-carbonate sample.

depositional age of the sediments and so may indicate the syngenetic introduction of hydrothermal fluids. This interpretation opens the exciting possibility of a hydrothermal Mo source into the Eoarchean ocean that may have been beneficial for early life (Schoepp-Cothenet et al., 2012). Alternatively, the molybdenite, including the sulfur, may have been introduced by metamorphism shortly after sediment deposition, consistent with the metamorphic history of the region (Ramírez-Salazar et al., 2021). The Neoarchean age agrees with a recently identified second metamorphic event (Eskesen et al., 2023) and likely represents partial recrystallization of the Eoarchean molybdenite. Metamorphic recrystallization is also evidenced from the textures (Figures 2 and 3). In the case of the meta-carbonates, we were not able to date sulfides, but the Rb-Sr ages of the mica (Figure 8d) agree with the Proterozoic ages of shear zones in the Mesoarchean Akia terrane of Greenland (Kirkland et al., 2023). This opens the possibility of metasomatic alteration associated with shearing at a post-Archean time.

If the hydrothermal fluid carried an MDF signature (i.e., no MIF), as one would expect for a magmatic or mantle-derived fluid, this would mix with the existing rock and act to weaken the MIF signal preserved in Archean sediments toward ~0‰ Δ^{33}S values (Papineau & Mojzsis, 2006). In contrast, a marine hydrothermal fluid from the Archean ocean would likely have the negative Δ^{33}S values that has been proposed for Archean seawater sulfate (Baumgartner et al., 2020) and may thus push sedimentary Δ^{33}S to negative values. If instead the fluid was derived from the post-Archean ocean, its Δ^{33}S composition would again have been zero and diluted any non-zero Δ^{33}S signatures. Lastly, it is possible that the hydrothermal fluid mobilized sedimentary sulfur from younger Archean rocks with a positive or negative MIF signature and deposited that sulfur in these Eoarchean strata, thereby introducing MIF into the Eoarchean strata analyzed in this study.

We cannot discount any of these possibilities and highlight that future in situ analyses would help to distinguish different generations of sulfides and potentially rule out different sources of sulfur

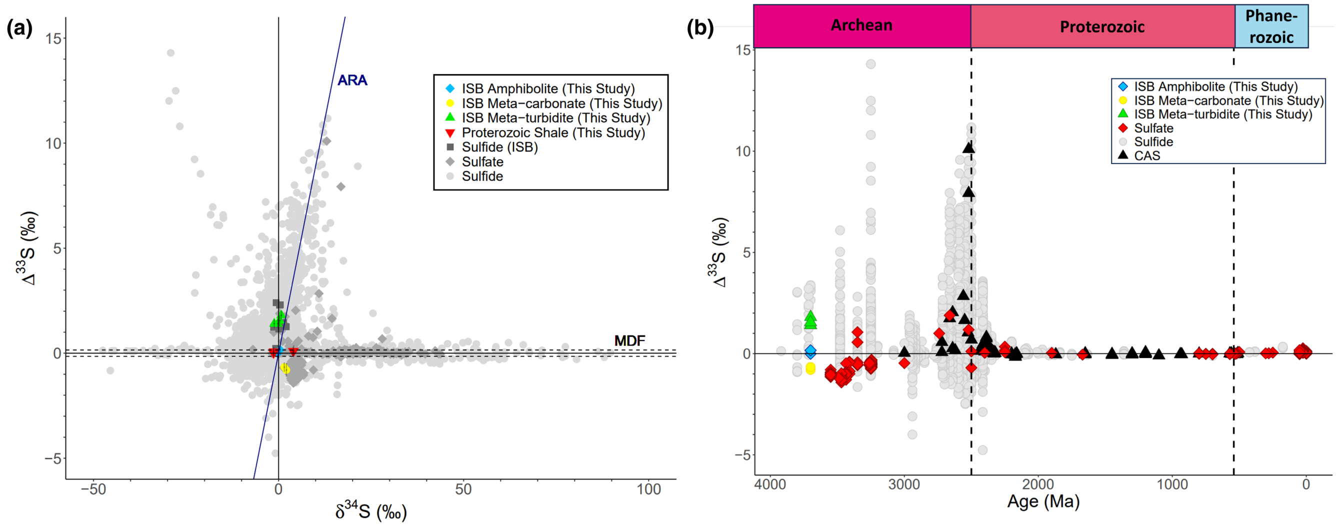

FIGURE 9 (a) Plot of δ^{34}S vs. Δ^{33}S for this study compared with sulfate and sulfide measurements through Earth history, taken from the compilation by Claire et al. (2014). ARA, Archean Reference Array; MDF, Mass Dependent Fractionation. (b) Compilation of Δ^{33}S values for sulfates, sulfides and CAS vs. time.

in these rocks. Nevertheless, there are reasons to believe that the meta-sedimentary rocks display primary MIF. First, the Eoarchean Re–Os age derived from the molybdenite suggests that at least some hydrothermal overprinting occurred during or shortly after sediment deposition. The molybdenum was likely sourced from the leaching of magmatic rocks, as marine and sedimentary Mo levels were very low at that time (Johnson et al., 2021). Hence the Δ^{33}S signature of this magmatic fluid would have been close to a magmatic value of zero per mil, and, therefore, the presence of MIF in the meta-turbidite is perhaps best explained by primary MIF-carrying sulfur in the sediments. Second, the amphibolite sample 207849C displayed significant veining and secondary sulfide emplacement, and yet the Δ^{33}S value of this sample falls just outside but within error of the MDF threshold with a Δ^{33}S value of 0.16‰. Both our amphibolite Δ^{33}S values are similar to the composition of previously measured amphibolites from the ISB (−0.17‰ to 0.26‰, average of 0.02‰, Siedenberg et al., 2016) and other Archean basalt from the Dresser Formation in western Australia (−0.100‰) and the Ameralik Dykes in the IGC (0.02‰) (Mojzsis et al., 2003; Ueno et al., 2008), indicating a magmatic sulfur source with Δ^{33}S of ~0‰. This contrasts with the larger Δ^{33}S values seen in the meta-turbidites and meta-carbonates. Collectively, our petrographic observations and isotopic results may thus indicate the presence of a primary MIF signal that was overprinted and perhaps somewhat muted by Archean and/or Proterozoic fluids that did not contain MIF. Further analyses would be needed to fully discount the possibility that some sulfur phases were introduced during Neoarchean or Palaeoproterozoic metamorphism (Eskesen et al., 2023).

6 | CONCLUSION AND IMPLICATIONS

To conclude, our sulfur isotope analysis of whole-rock samples by MC-ICP-MS is both accurate and precise. This method can, therefore, become an important new addition to the geochemical toolbox as it opens up analyses of multiple sulfur isotopes in rock samples with very low sulfur content where NanoSIMS or miniaturized fluorination techniques are not available. Although this method cannot distinguish between individual sulfide phases, the distinct patterns that we identified between the different localities indicate that it can nevertheless provide important new insights into the predominant sulfur sources in a given sample set.

ISB meta-turbidites exhibit a positive MIF signature characteristic of Archean sulfides formed in a low oxygen atmosphere, in line with previous analyses of schists and BIFs in the ISB. Pyrite, as well as chalcopyrite and in one case molybdenite, were likely the main sulfur host mineral in these samples. The presence of chalcopyrite and molybdenite, along with textural observations, suggests the input of hydrothermal fluids, either during or after sediment deposition. The Re–Os date obtained from the molybdenite points to at least one Eoarchean fluid injection event, followed by recrystallization during the Neoarchean (cf. Eskesen et al., 2023). The chalcopyrite remains undated. We therefore cannot rule out the possibility that these hydrothermal fluids also introduced the MIF signal, mobilized from younger Archean sedimentary strata; however, a primary origin remains possible.

The ISB meta-carbonates exhibit a negative MIF signature of a similar magnitude to previously measured Archean barites. However, the *aqua regia* digestion method does not fully attack barite, and sulfides were more prevalent in the samples analyzed. The most likely host phase of sulfur in these rocks was pyrite. Its negative Δ^{33}S signature is most parsimoniously explained by the reduction of marine sulfate, similar to what has been described from slightly younger Paleoarchean rocks (Roerdink et al., 2013; Ueno et al., 2008). Nearby amphibolites, despite evidence of secondary fluid infiltration, do not show significant MIF, suggesting that at least the secondary sulfur in those samples had a magmatic source. New Rb–Sr data reveal a Proterozoic age for micas in the meta-carbonate, potentially indicating a shearing event and possibly metasomatic alteration at that time (cf. Kirkland et al., 2023). Hence it is conceivable that the meta-sedimentary rocks initially contained a large MIF signal that was perhaps reduced in magnitude by magmatic hydrothermal overprinting. In this case, some of the measured MIF would be primary in origin and reflective of a sedimentary depositional environment under an anoxic Archean atmosphere.

In conclusion, the rock units that we investigated, and which contain some of the most famous Eoarchean biosignatures, nurture the idea that volcanism could have supplied key metabolites in the form of sulfur and possibly trace metals (including molybdenum, as indicated by the molybdenite vein) to the early biosphere. Our findings support the notion that a volcanically active planet may facilitate habitability.

ACKNOWLEDGMENTS

Financial support was provided by a NERC Frontiers grant to EES (NE/V010824/1). Heidi Block, Stuart Allison, and Sebastian Fischer (University of St Andrews) are thanked for their technical support. The geochronology analyses at The University of Adelaide were supported by an Australian Research Council Future Fellowship (FT210100906). We thank Carsten Münker for organizing the field trip to the Isua carbonate locality in Summer 2022.

FUNDING INFORMATION

Financial support was provided by a NERC Frontiers grant to EES (NE/V010824/1). The geochronology analyses at The University of Adelaide were supported by an Australian Research Council Future Fellowship (FT210100906).

CONFLICT OF INTEREST STATEMENT

We have no competing interests to declare.

DATA AVAILABILITY STATEMENT

All data associated with this project are provided in the data tables in the main text and in the supplementary files.

ORCID

Jane E. Macdonald https://orcid.org/0009-0008-7644-4173
Kristoffer Szilas https://orcid.org/0000-0002-5541-306X
Eva E. Stüeken https://orcid.org/0000-0001-6861-2490

REFERENCES

Abbasi, S., Lamb, D. T., Palanisami, T., Kader, M., Matanitobua, V., Megharaj, M., & Naidu, R. (2016). Bioaccessibility of barium from barite contaminated soils based on gastric phase in vitro data and plant uptake. *Chemosphere*, *144*, 1421–1427. https://doi.org/10.1016/j.chemosphere.2015.10.031

Albarède, F. (2011). Fractionation, mass independent and dependent. In R. Amils, et al. (Eds.), *Encyclopedia of astrobiology* (pp. 611–612). Springer. https://doi.org/10.1007/978-3-642-27833-4_597-2

Allwood, A. C., Rosing, M. T., Flannery, D. T., Hurowitz, J. A., & Heirwegh, C. M. (2018). Reassessing evidence of life in 3,700-million-year-old rocks of Greenland. *Nature*, *563*(7730), 241–244. https://doi.org/10.1038/s41586-018-0610-4

Anbar, A. D., & Knoll, A. H. (2002). Proterozoic ocean chemistry and evolution: A bioinorganic bridge? *Science*, *297*(5584), 1137–1142. https://doi.org/10.1126/science.1069651

Appel, P. W. U., Fedo, C. M., Moorbath, S., & Myers, J. S. (1998). Recognizable primary volcanic and sedimentary features in a low-strain domain of the highly deformed, oldest known (~3.7–3.8 Gyr) Greenstone Belt, Isua, West Greenland. *Terra Nova*, *10*(2), 57–62. https://doi.org/10.1046/j.1365-3121.1998.00162.x

Au Yang, D., Landais, G., Assayag, N., Widory, D., & Cartigny, P. (2016). Improved analysis of micro-and nanomole-scale sulfur multi-isotope compositions by gas source isotope ratio mass spectrometry. *Rapid Communications in Mass Spectrometry*, *30*(7), 897–907.

Bao, H., Rumble, D., & Lowe, D. R. (2007). The five stable isotope compositions of Fig Tree barites: Implications on sulfur cycle in ca. 3.2Ga oceans. *Geochimica et Cosmochimica Acta*, *71*(20), 4868–4879. https://doi.org/10.1016/j.gca.2007.05.032

Baumgartner, R. J., Caruso, S., Fiorentini, M. L., van Kranendonk, M. J., Martin, L., Jeon, H., Pagès, A., & Wacey, D. (2020). Sulfidization of 3.48 billion-year-old stromatolites of the Dresser Formation, Pilbara Craton: Constraints from in-situ sulfur isotope analysis of pyrite. *Chemical Geology*, *538*, 119488. https://doi.org/10.1016/j.chemgeo.2020.119488

Black, L. (2007). SHRIMP U–Pb zircon ages obtained during 2006/07 for NSW geological survey projects. *Geological Survey of New South Wales*, Report GS2007/298.

Boak, J. L., & Dymek, R. F. (1982). Metamorphism of the ca. 3800 Ma supracrustal rocks at Isua, West Greenland: Implications for early Archaean crustal evolution. *Earth and Planetary Science Letters*, *59*(1), 155–176. https://doi.org/10.1016/0012-821X(82)90123-6

Böttcher, M. E., Brumsack, H. J., & Dürselen, C. D. (2007). The isotopic composition of modern seawater sulfate: I. Coastal waters with special regard to the North Sea. *Journal of Marine Systems*, *67*(1–2), 73–82. https://doi.org/10.1016/j.jmarsys.2006.09.006

Brand, W. A., Coplen, T. B., Vogl, J., Rosner, M., & Prohaska, T. (2014). Assessment of international reference materials for isotope-ratio analysis (IUPAC technical report). *Pure and Applied Chemistry*, *86*(3), 425–467. https://doi.org/10.1515/pac-2013-1023

Bruker. (2023). *Lab report XRF 456*. Analysis of geological thin sections.

Bryant, R. N., Jones, C., Raven, M. R., Gomes, M. L., Berelson, W. M., Bradley, A. S., & Fike, D. A. (2019). Sulfur isotope analysis of microcrystalline iron sulfides using secondary ion mass spectrometry imaging: Extracting local paleo-environmental information from modern and ancient sediments. *Rapid Communications in Mass Spectrometry*, *33*(5), 491–502.

Bucholz, C. E., Biasi, J. A., Beaudry, P., & Ono, S. (2020). Sulfur isotope behavior during metamorphism and anatexis of Archean sedimentary rocks: A case study from the Ghost Lake batholith, Ontario, Canada. *Earth and Planetary Science Letters*, *549*, 116494. https://doi.org/10.1016/j.epsl.2020.116494

Burke, A., Moore, K. A., Sigl, M., Nita, D. C., McConnell, J. R., & Adkins, J. F. (2019). Stratospheric eruptions from tropical and extra-tropical volcanoes constrained using high-resolution sulfur isotopes in ice cores. *Earth and Planetary Science Letters*, *521*, 113–119. https://doi.org/10.1016/j.epsl.2019.06.006

Burke, A., Present, T. M., Paris, G., Rae, E. C. M., Sandilands, B. H., Gaillardet, J., Peucker-Ehrenbrink, B., Fischer, W. W., McClelland, J. W., Spencer, R. G. M., Voss, B. M., & Adkins, J. F. (2018). Sulfur isotopes in rivers: Insights into global weathering budgets, pyrite oxidation, and the modern sulfur cycle. *Earth and Planetary Science Letters*, *496*, 168–177. https://doi.org/10.1016/j.epsl.2018.05.022

Cai, C., Li, H., Li, K., & Wang, D. (2022). Thermochemical sulfate reduction in sedimentary basins and beyond: A review. *Chemical Geology*, *607*, 121018.

Cao, S., Neubauer, F., Bernroider, M., Genser, J., Liu, J., & Friedl, G. (2017). Low-grade retrogression of a high-temperature metamorphic core complex: Naxos, Cyclades, Greece. *Bulletin of the Geological Society of America*, *129*(1–2), 93–117. https://doi.org/10.1130/B31502.1

Chipman, D. W. (1989). Retrograde metamorphism. In D. R. Bowes (Ed.), *The encyclopedia of igneous and metamorphic petrology* (pp. 509–511). Van Nostrand Reinhold.

Claire, M. W., Kasting, J. F., Domagal-Goldman, S. D., Stüeken, E. E., Buick, R., & Meadows, V. S. (2014). Modeling the signature of sulfur mass-independent fractionation produced in the Archean atmosphere. *Geochimica et Cosmochimica Acta*, *141*, 365–380. https://doi.org/10.1016/j.gca.2014.06.032

Crowe, S. A., Paris, G., Katsev, S., Jones, C., Kim, S.-T., Zerkle, A. L., Nomosatryo, S., Fowle, D. A., Adkins, J. F., Sessions, A. L., Farquhar, J., & Canfield, D. E. (2014). Sulfate was a trace constituent of Archean seawater. *Science*, *346*(6210), 735–739. https://doi.org/10.1126/science.1258966

Cui, H., Kitajima, K., Spicuzza, M. J., Fournelle, J. H., Ishida, A., Brown, P. E., & Valley, J. W. (2018). Searching for the great oxidation event in North America: A reappraisal of the Huronian supergroup by SIMS sulfur four-isotope analysis. *Astrobiology*, *18*(5), 519–538. https://doi.org/10.1089/ast.2017.1722

Endo, Y., Danielache, S. O., Ogawa, M., & Ueno, Y. (2022). Absorption spectra measurements at ~1 cm^{-1} spectral resolution of ^{32}S, ^{33}S, ^{34}S, and ^{36}S sulfur dioxide for the 206–220 nm region and applications to modeling of the isotopic self-shielding. *Geochemical Journal*, *56*(1), 40–56.

Eskesen, B., Fassmer, K., Münker, C., Ulrich, T., Szilas, K., Wagner, S., Hoffmann, J. E., & Nagel, T. J. (2023). Neoarchean synkinematic metamorphic peak in the Isua Supracrustal Belt (West Greenland). *Geology*, *51*(11), 1017–1021. https://doi.org/10.1130/G51564.1

Farquhar, J., Bao, H., & Thiemens, M. (2000). Atmospheric influence of earth's earliest sulfur cycle. *Science*, *289*(5480), 756–758. https://doi.org/10.1126/science.289.5480.756

Farquhar, J., Savarino, J., Airieau, S., & Thiemens, M. H. (2001). Observation of wavelength-sensitive mass-independent sulfur isotope effects during SO_2 photolysis: Implications for the early atmosphere. *Journal of Geophysical Research: Planets*, *106*(E12), 32829–32839. https://doi.org/10.1029/2000JE001437

Farquhar, J., & Wing, B. A. (2003). Multiple sulfur isotopes and the evolution of the atmosphere. *Earth and Planetary Science Letters*, *213*(1–2), 1–13. https://doi.org/10.1016/S0012-821X(03)00296-6

Flude, S., Haschke, M., Storey, M., & Harvey, J. (2017). Application of benchtop micro-XRF to geological materials. *Mineralogical Magazine*, *81*(4), 923–948. https://doi.org/10.1180/minmag.2016.080.150

Gilbert, S., Danyushevsky, L., Robinson, P., Wohlgemuth-Ueberwasser, C., Pearson, N., Savard, D., Norman, M., & Hanley, J. (2013). A comparative study of five reference materials and the Lombard meteorite for the determination of the platinum-group elements and gold by LA-ICP-MS. *Geostandards and Geoanalytical Research*, *37*(1), 51–64. https://doi.org/10.1111/j.1751-908X.2012.00170.x

Glorie, S., Gilbert, S., Hand, M., & Lloyd, J. (2024). Calibration methods for laser ablation Rb–Sr geochronology: Comparisons and recommendation based on NIST glass and natural reference materials. *Geochronology*, *6*(1), 21–36. https://doi.org/10.5194/egusphere-2023-1915

Glorie, S., Hand, M., Mulder, J., Simpson, A., Emo, R. B., Kamber, N., Fernie, N., Nixon, A., & Gilbert, S. (2024). Robust laser ablation Lu–Hf dating of apatite: An empirical evaluation. *Geological Society, London, Special Publications*, *537*(1), 165–184. https://doi.org/10.1144/SP537-2022-205

Haldar, S. K. (2017). Platinum-nickel-chromium deposits. In *Platinum-nickel-chromium deposits: Geology, exploration and reserve base* (pp. 1–35). Elsevier.

Halevy, I. (2013). Production, preservation, and biological processing of mass-independent sulfur isotope fractionation in the Archean surface environment. *Proceedings of the National Academy of Sciences*, *110*(44), 17644–17649.

Harman, C. E., Pavlov, A. A., Babikov, D., & Kasting, J. F. (2018). Chain formation as a mechanism for mass-independent fractionation of sulfur isotopes in the Archean atmosphere. *Earth and Planetary Science Letters*, *496*, 238–247.

Hogmalm, K. J., Dahlgren, I., Fridolfsson, I., & Zack, T. (2019). First in situ Re–Os dating of molybdenite by LA-ICP-MS/MS. *Mineralium Deposita*, *54*, 821–828. https://doi.org/10.1007/s00126-019-00889-1

Hogmalm, K. J., Zack, T., Karlsson, A. K. O., Sjoqvist, A. S. L., & Garbe-Schonberg, D. (2017). In situ Rb–Sr and K–Ca dating by LA-ICP-MS/MS: An evaluation of N_2O and SF_6 as reaction gases. *Journal of Analytical Atomic Spectrometry*, *32*(2), 305–313. https://doi.org/10.1039/C6JA00362A

Hu, Z., Gao, S., Liu, Y., Hu, S., Chen, H., & Yuan, H. (2008). Signal enhancement in laser ablation ICP-MS by addition of nitrogen in the central channel gas. *Journal of Analytical Atomic Spectrometry*, *23*(8), 1093–1101. https://doi.org/10.1039/b804760j

Hulston, J. R., & Thode, H. G. (1965). Variations in the S^{33}, S^{34}, and S^{36} contents of meteorites and their relation to chemical and nuclear effects. *Journal of Geophysical Research*, *70*(14), 3475–3484. https://doi.org/10.1029/JZ070i014p03475

Janssens, K. H., Adams, F., & Rindby, A. (2000). *Microscopic X-ray fluorescence analysis* (Vol. 434). Wiley.

Johnson, A. C., Ostrander, C. M., Romaniello, S. J., Reinhard, C. T., Greaney, A. T., Lyons, T. W., & Anbar, A. D. (2021). Reconciling evidence of oxidative weathering and atmospheric anoxia on Archean earth. *Science Advances*, *7*(40), eabj0108. https://doi.org/10.1126/sciadv.abj0108

Johnston, D. T. (2011). Multiple sulfur isotopes and the evolution of earth's surface sulfur cycle. *Earth-Science Reviews*, *106*(1–2), 161–183. https://doi.org/10.1016/j.earscirev.2011.02.003

Kamber, B. S., & Whitehouse, M. J. (2007). Micro-scale sulphur isotope evidence for sulphur cycling in the late Archean shallow ocean. *Geobiology*, *5*(1), 5–17.

Kaufman, A. J., Johnston, D. T., Farquhar, J., Masterson, A. L., Lyons, T. W., Bates, S., Anbar, A. D., Arnold, G. L., Garvin, J., & Buick, R. (2007). Late Archean biospheric oxygenation and atmospheric evolution. *Science*, *317*(5846), 1900–1903.

Kemeny, P. C., Torres, M. A., Lamb, M. P., Webb, S. M., Dalleska, N., Cole, T., Hou, Y., Marske, J., Adkins, J. F., & Fischer, W. W. (2021). Organic sulfur fluxes and geomorphic control of sulfur isotope ratios in rivers. *Earth and Planetary Science Letters*, *562*, 116838. https://doi.org/10.1016/j.epsl.2021.116838

Kirkland, C. L., Olierook, H. K., Danišík, M., Liebmann, J., Hollis, J., Ribeiro, B. V., & Rankenburg, K. (2023). Dating mylonitic overprinting of ancient rocks. *Communications Earth & Environment*, *4*(1), 47. https://doi.org/10.1038/s43247-023-00709-5

Kolb, J., Bagas, L., & Fiorentini, M. L. (2015). Metallogeny of the North Atlantic craton in Greenland. *Mineralogical Magazine*, *79*(4), 815–855. https://doi.org/10.1180/minmag.2015.079.4.01

Košler, J., Simonetti, A., Sylvester, P. J., Cox, R. A., Tubrett, M. N., & Wilton, D. H. C. (2003). Laser-ablation ICP–MS measurements of Re/Os in molybdenite and implications for Re–Os geochronology. *The Canadian Mineralogist*, *41*(2), 307–320. https://doi.org/10.2113/gscanmin.41.2.307

Marin-Carbonne, J., Decraene, M. N., Havas, R., Remusat, L., Pasquier, V., Alléon, J., Zeyen, N., Bouton, A., Bernard, S., Escrig, S., & Olivier, N. (2022). Early precipitated micropyrite in microbialites: A time capsule of microbial sulfur cycling. *Geochemical Perspectives Letters*, *21*, 7–12.

McGregor, V. R., & Mason, B. (1977). Petrogenesis and geochemistry of metabasaltic and metasedimentary enclaves in the Amitsoq gneisses, West Greenland. *American Mineralogist*, *62*(9–10), 887–904.

McLennan, S. M. (1989). Rare earth elements in sedimentary rocks; influence of provenance and sedimentary processes. *Reviews in Mineralogy and Geochemistry*, *21*(1), 169–200.

Mishima, K., Yamazaki, R., Satish-Kumar, M., Ueno, Y., Hokada, T., & Toyoshima, T. (2017). Multiple sulfur isotope geochemistry of Dharwar Supergroup, Southern India: Late Archean record of changing atmospheric chemistry. *Earth and Planetary Science Letters*, *464*, 69–83.

Mojzsis, S. J., Arrhenius, G., McKeegan, K. D., Harrison, T. M., Nutman, A. P., & Friend, C. R. L. (1996). Evidence for life on earth before 3,800 million years ago. *Nature*, *384*(6604), 55–59.

Mojzsis, S. J., Coath, C. D., Greenwood, J. P., McKeegan, K. D., & Harrison, T. M. (2003). Mass-independent isotope effects in Archean (2.5–3.8 Ga) sedimentary sulfides determined by ion microprobe analysis. *Geochimica et Cosmochimica Acta*, *67*(9), 1635–1658. https://doi.org/10.1016/S0016-7037(03)00059-0

Morrison, P. R., & Mojzsis, S. J. (2020). Tracing the early emergence of microbial sulfur metabolisms. *Geomicrobiology Journal*, *38*(1), 1–21. https://doi.org/10.1080/01490451.2020.1812773

Muller, É., Philippoa, P., Rollion-Bard, C., & Cartigny, P. (2016). Multiple sulfur-isotope signatures in archean sulfates and their implications for the chemistry and dynamics of the early atmosphere. *Proceedings of the National Academy of Sciences of the United States of America*, *113*(27), 7432–7437. https://doi.org/10.1073/pnas.1520522113

Nakano, K. (2018). *Ultra-low level determination of phosphorus, sulfur, silicon and chlorine using the Agilent 8900 ICP-QQQ*. Agilent application note, 2018. 5991-6852EN.

Nielson, G. C., Stüeken, E. E., & Prave, A. R. (2024). Estuaries house Earth's oldest known non-marine eukaryotes. *Precambrian Research*, *401*, 107278. https://doi.org/10.1016/j.precamres.2023.107278

Norris, A., & Danyushevsky, L. (2018). *Towards estimating the complete uncertainty budget of quantified results measured by LA-ICP-MS*. Goldschmidt.

Nutman, A. P., & Friend, C. R. L. (2009). New 1:20,000 scale geological maps, synthesis and history of investigation of the Isua Supracrustal Belt and adjacent orthogneisses, southern West Greenland: A glimpse of Eoarchaean crust formation and orogeny. *Precambrian Research*, *172*(3–4), 189–211. https://doi.org/10.1016/j.precamres.2009.03.017

Nutman, A. P., Bennett, V. C., Friend, C. R. L., van Kranendonk, M. J., & Chivas, A. R. (2016). Rapid emergence of life shown by discovery of 3,700-million-year-old microbial structures. *Nature*, *537*(7621), 535–538. https://doi.org/10.1038/nature19355

Nutman, A. P., Friend, C. R., & Bennett, V. C. (2002). Evidence for 3650–3600 Ma assembly of the northern end of the Itsaq Gneiss Complex, Greenland: Implication for early Archaean tectonics. *Tectonics*, *21*(1), 5-1–5-28. https://doi.org/10.1029/2000TC001203

Nutman, A. P., Friend, C. R., Bennett, V. C., Yi, K., & Van Kranendonk, M. (2022). Review of the Isua Supracrustal Belt area (Greenland) Eoarchean geology from integrated 1:20,000 scale maps, field observations and laboratory data: Constraints on early geodynamics. *Precambrian Research*, *379*, 106785. https://doi.org/10.1016/j.precamres.2022.106785

Nutman, A. P., Friend, C. R., Kinny, P. D., & McGregor, V. R. (1993). Anatomy of an early Archean Gneiss Complex: 3900 to 3600 Ma crustal evolution in southern West Greenland. *Geology*, *21*(5), 415–418. https://doi.org/10.1130/0091-7613(1993)021<0415:AOAEAG>2.3.CO;2

Nutman, A. P., McGregor, V. R., Friend, C. R., Bennett, V. C., & Kinny, P. D. (1996). The Itsaq Gneiss Complex of southern West Greenland; the world's most extensive record of early crustal evolution (3900–3600 Ma). *Precambrian Research*, *78*(1–3), 1–39. https://doi.org/10.1016/0301-9268(95)00066-6

Oduro, H., Harms, B., Sintim, H. O., Kaufman, A. J., Cody, G., & Farquhar, J. (2011). Evidence of magnetic isotope effects during thermochemical sulfate reduction. *Proceedings of the National Academy of Sciences*, *108*(43), 17635–17638.

Ohtomo, Y., Kakegawa, T., Ishida, A., Nagase, T., & Rosing, M. T. (2014). Evidence for biogenic graphite in early Archaean Isua metasedimentary rocks. *Nature Geoscience*, *7*(1), 25–28.

Ono, S., Eigenbrode, J. L., Pavlov, A. A., Kharecha, P., Rumble, D., Kasting, J. F., & Freeman, K. H. (2003). New insights into Archean sulfur cycle from mass-independent sulfur isotope records from the Hamersley Basin, Australia. *Earth and Planetary Science Letters*, *213*(1–2), 15–30. https://doi.org/10.1016/S0012-821X(03)00295-4

Ono, S., Wing, B., Rumble, D., & Farquhar, J. (2006). High precision analysis of all four stable isotopes of sulfur (32S, 33S, 34S and 36S) at nanomole levels using a laser fluorination isotope-ratio-monitoring gas chromatography-mass spectrometry. *Chemical Geology*, *225*(1–2), 30–39. https://doi.org/10.1016/j.chemgeo.2005.08.005

Papineau, D., & Mojzsis, S. (2006). Mass-independent fractionation of sulfur isotopes in sulfides from the pre-3770 Isua Supracrustal Belt, West Greenland. *Geobiology*, *4*(4), 227–238. https://doi.org/10.1111/j.1472-4669.2006.00083.x

Paris, G., Adkins, J. F., Sessions, A. L., Webb, S. M., & Fischer, W. W. (2014). Neoarchean carbonate-associated sulfate records positive δ^{33}S anomalies. *Science*, *346*(6210), 739–741. https://doi.org/10.1126/science.1258211

Paris, G., Fehrenbacher, J. S., Sessions, A. L., Spero, H. J., & Adkins, J. F. (2014). Experimental determination of carbonate-associated sulfate δ^{34}S in planktonic foraminifera shells. *Geochemistry, Geophysics, Geosystems*, *15*(4), 1452–1461. https://doi.org/10.1002/2014GC005295

Paris, G., Sessions, A. L., Subhas, A. V., & Adkins, J. F. (2013). MC-ICP-MS measurement of δ^{34}S and Δ^{33}S in small amounts of dissolved sulfate. *Chemical Geology*, *345*, 50–61. https://doi.org/10.1016/j.chemgeo.2013.02.022

Pavlov, A. A., & Kasting, J. F. (2002). Mass-independent fractionation of sulfur isotopes in Archean sediments: Strong evidence for an anoxic Archean atmosphere. *Astrobiology*, *2*(1), 27–41. https://doi.org/10.1089/153110702753621321

Pichler, H., & Schmitt-Riegraf, C. (1997). *Rock-forming minerals in thin section* (pp. 79–167). Springer Netherlands.

Polat, A., & Hofmann, A. W. (2003). Alteration and geochemical patterns in the 3.7–3.8 Ga Isua Greenstone Belt, West Greenland. *Precambrian Research*, *126*(3–4), 197–218. https://doi.org/10.1016/S0301-9268(03)00095-0

Present, T. M., Paris, G., Burke, A., Fischer, W. W., & Adkins, J. F. (2015). Large Carbonate Associated Sulfate isotopic variability between brachiopods, micrite, and other sedimentary components in Late Ordovician strata. *Earth and Planetary Science Letters*, *432*, 187–198. https://doi.org/10.1016/j.epsl.2015.10.005

Ptáček, M. P., Dauphas, N., & Greber, N. D. (2020). Chemical evolution of the continental crust from a data-driven inversion of terrigenous sediment compositions. *Earth and Planetary Science Letters*, *539*, 116090. https://doi.org/10.1016/j.epsl.2020.116090

Raiswell, R., Hardisty, D. S., Lyons, T. W., Canfield, D. E., Owens, J. D., Planavsky, N. J., Poulton, S. W., & Reinhard, C. T. (2018). The iron paleoredox proxies: A guide to the pitfalls, problems and proper practice. *American Journal of Science*, *318*(5), 491–526. https://doi.org/10.2475/05.2018.03

Ramírez-Salazar, A., Müller, T., Piazolo, S., Webb, A. A. G., Hauzenberger, C., Zuo, J., Haproff, P., Harvey, J., Wong, T. K., & Charlton, C. (2021). Tectonics of the Isua Supracrustal Belt 1: P-T-X-d constraints of a poly-metamorphic terrane. *Tectonics*, *40*(3), e2020TC006516. https://doi.org/10.1029/2020TC006516

Redaa, A., Farkaš, J., Gilbert, S., Collins, A. S., Wade, B., Löhr, S., Zack, T., & Garbe-Schönberg, D. (2021). Assessment of elemental fractionation and matrix effects during in situ Rb–Sr dating of phlogopite by

LA-ICP-MS/MS: Implications for the accuracy and precision of mineral ages. *Journal of Analytical Atomic Spectrometry*, *36*(2), 322–344. https://doi.org/10.1039/D0JA00299B

Rennie, V. C. F., Paris, G., Sessions, A. L., Abramovich, S., Turchyn, A. V., & Adkins, J. F. (2018). Cenozoic record of δ34S in foraminiferal calcite implies an early Eocene shift to deep-ocean sulfide burial. *Nature Geoscience*, *11*(10), 761–765. https://doi.org/10.1038/s41561-018-0200-y

Roerdink, D. L., Mason, P. R., Whitehouse, M. J., & Reimer, T. (2013). High-resolution quadruple sulfur isotope analyses of 3.2 Ga pyrite from the Barberton Greenstone Belt in South Africa reveal distinct environmental controls on sulfide isotopic arrays. *Geochimica et Cosmochimica Acta*, *117*, 203–215.

Roerdink, D. L., Mason, P. R. D., Farquhar, J., & Reimer, T. (2012). Multiple sulfur isotopes in Paleoarchean barites identify an important role for microbial sulfate reduction in the early marine environment. *Earth and Planetary Science Letters*, *331–332*, 177–186. https://doi.org/10.1016/j.epsl.2012.03.020

Rose, N. M., Rosing, M. T., & Bridgwater, D. (1996). The origin of metacarbonate rocks in the Archaean Isua Supracrustal Belt, West Greenland. *American Journal of Science*, *296*(9), 1004–1044. https://doi.org/10.2475/ajs.296.9.1004

Rosing, M. T. (1999). ^{13}C-depleted carbon microparticles in ≥3700-Ma sea-floor sedimentary rocks from west Greenland. *Science*, *283*(5402), 674–676. https://doi.org/10.1126/science.283.5402.674

Rudnick, R. L., & Gao, S. (2014). Composition of continental crust. *Treatise Geochem*, *4*, 1–51. https://doi.org/10.1016/B0-08-043751-6/03016-4

Schier, K., Bau, M., Smith, A. J. B., Beukes, N. J., Coetzee, L. L., & Viehmann, S. (2020). Chemical evolution of seawater in the Transvaal Ocean between 2426 ma (Ongeluk large Igneous Province) and 2413 ma ago (Kalahari Manganese Field). *Gondwana Research*, *88*, 373–388. https://doi.org/10.1016/j.gr.2020.09.001

Schoepp-Cothenet, B., Van Lis, R., Philippot, P., Magalon, A., Russell, M. J., & Nitschke, W. (2012). The ineluctable requirement for the trans-iron elements molybdenum and/or tungsten in the origin of life. *Scientific Reports*, *2*(1), 263. https://doi.org/10.1038/srep00263

Schurr, S. L., Genske, F., Strauss, H., & Stracke, A. (2020). A comparison of sulfur isotope measurements of geologic materials by inductively coupled plasma and gas source mass spectrometry. *Chemical Geology*, *558*, 119869. https://doi.org/10.1016/j.chemgeo.2020.119869

Shabani, A. A. T. (2009). Mineral chemistry of chlorite replacing biotite from granitic rocks of the Canadian Appalachians. *Journal of Sciences, Islamic Republic of Iran*, *20*(3), 265–275.

Siedenberg, K., Strauss, H., & Hoffmann, E. J. (2016). Multiple sulfur isotope signature of early Archean oceanic crust, Isua (SW-Greenland). *Precambrian Research*, *283*, 1–12. https://doi.org/10.1016/j.precamres.2016.07.002

Sim, M. S., Bosak, T., & Ono, S. (2011). Large sulfur isotope fractionation does not require disproportionation. *Science*, *333*(6038), 74–77.

Stüeken, E. E., Boocock, T., Szilas, K., Mikhail, S., & Gardiner, N. J. (2021). Reconstructing nitrogen sources to earth's earliest biosphere at 3.7 Ga. *Frontiers in Earth Science*, *9*, 675726. https://doi.org/10.3389/feart.2021.675726

Tamblyn, R., Gilbert, S., Glorie, S., Spandler, C., Simpson, A., Hand, M., Hasterok, D., Ware, B., & Tessalina, S. (2024). Molybdenite reference materials for in situ LA–ICP–MS/MS Re–Os geochronology. *Geostandards and Geoanalytical Research* in press.

Ueno, Y., Ono, S., Rumble, D., & Maruyama, S. (2008). Quadruple sulfur isotope analysis of ca. 3.5 Ga dresser formation: New evidence for microbial sulfate reduction in the early Archean. *Geochimica et Cosmochimica Acta*, *72*(23), 5675–5691.

Vermeesch, P. (2018). IsoplotR: A free and open toolbox for geochronology. *Geoscience Frontiers*, *9*(5), 1479–1493. https://doi.org/10.1016/j.gsf.2018.04.001

Viehmann, S., Bau, M., Hoffmann, J. E., & Münker, C. (2015). Geochemistry of the Krivoy Rog Banded Iron Formation, Ukraine, and the impact of peak episodes of increased global magmatic activity on the trace element composition of Precambrian seawater. *Precambrian Research*, *270*, 165–180. https://doi.org/10.1016/j.precamres.2015.09.015

Villa, I. M., De Bièvre, P., Holden, N. E., & Renne, P. R. (2015). IUPAC-IUGS recommendation on the half life of ^{87}Rb. *Geochimica et Cosmochimica Acta*, *164*, 382–385. https://doi.org/10.1016/j.gca.2015.05.025

Wacey, D. (2010). Stromatolites in the ~3400 Ma Strelley Pool Formation, Western Australia: Examining biogenicity from the macro- to the nano-scale. *Astrobiology*, *10*(4), 381–395. https://doi.org/10.1089/ast.2009.0423

Wenk, H. R., & Bulakh, A. (2016). *Minerals: Their constitution and origin*. Cambridge University Press.

White, W. M., & Klein, E. M. (2014). 4.13-composition of the oceanic crust. In H. D. Holland & K. K. Turekian (Eds.), *Treatise on geochemistry* (2nd ed., pp. 457–496). Elsevier. https://doi.org/10.1016/B978-0-08-095975-7.00315-6

Whitehill, A. R., Jiang, B., Guo, H., & Ono, S. (2015). SO_2 photolysis as a source for sulfur mass-independent isotope signatures in stratospehric aerosols. *Atmospheric Chemistry and Physics*, *15*(4), 1843–1864. https://doi.org/10.5194/acp-15-1843-2015

Whitehouse, M. J., Kamber, B. S., Fedo, C. M., & Lepland, A. (2005). Integrated Pb-and S-isotope investigation of sulphide minerals from the early Archaean of southwest Greenland. *Chemical Geology*, *222*(1–2), 112–131.

Xu, G., Hannah, J. L., Bingen, B., Georgiev, S., & Stein, H. J. (2012). Digestion methods for trace element measurements in shales: Paleoredox proxies examined. *Chemical Geology*, *324–325*, 132–147. https://doi.org/10.1016/j.chemgeo.2012.01.029

Zawaski, M. J., Kelly, N. M., Orlandini, O. F., Nichols, C. I. O., Allwood, A. C., & Mojzsis, S. J. (2020). Reappraisal of purported ca. 3.7 Ga stromatolites from the Isua Supracrustal Belt (West Greenland) from detailed chemical and structural analysis. *Earth and Planetary Science Letters*, *545*, 116409. https://doi.org/10.1016/j.epsl.2020.116409

Zuo, J., Webb, A. A. G., Piazolo, S., Wang, Q., Müller, T., Ramírez-Salazar, A., & Haproff, P. J. (2021). Tectonics of the Isua Supracrustal Belt 2: Microstructures reveal distributed strain in the absence of major fault structures. *Tectonics*, *40*(3), e2020TC006514. https://doi.org/10.1029/2020TC006514

SUPPORTING INFORMATION

Additional supporting information can be found online in the Supporting Information section at the end of this article.

How to cite this article: Macdonald, J. E., Sugden, P., Dumont, M., Szilas, K., Glorie, S., Simpson, A., Gilbert, S., Burke, A., & Stüeken, E. E. (2024). Evaluating the multiple sulfur isotope signature of Eoarchean rocks from the Isua Supracrustal Belt (Southwest-Greenland) by MC-ICP-MS: Volcanic nutrient sources for early life. *Geobiology*, *22*, e12595. https://doi.org/10.1111/gbi.12595